# Satellite stem cell dysfunction in Duchenne muscular dystrophy

Jules A. Granet[1], Rebecca Robertson[1], Romina L. Filippelli[1], Alessio Cusmano[1], Shulei Li[1], Moein Yaqubi[2], Jo Anne Stratton[2], Natasha C. Chang[1*]

[1]Department of Biochemistry, McGill University, Montréal, Québec, Canada.
[2]Department of Neurology and Neurosurgery, Montreal Neurological Institute, McGill University, Montréal, Québec, Canada
*Corresponding author: natasha.chang@mcgill.ca

## Abstract

Satellite cells are muscle-resident stem cells that maintain and repair muscle. Increasing evidence supports the contributing role of satellite cells in Duchenne muscular dystrophy (DMD), a lethal degenerative muscle disease caused by loss of dystrophin. We used single cell RNA-sequencing (scRNA-seq) to determine how dystrophin deficiency impacts satellite cell heterogeneity and function. scRNA-seq was performed in satellite cells from *mdx* and D2-*mdx* DMD mouse models. DMD satellite cells were disproportionally found within myogenic progenitor clusters and a unique DMD enriched cluster. DMD satellite cells and myogenic progenitors exhibited distinct impairments, including cell death and senescence, respectively. Moreover, dystrophic satellite cells express an impaired myogenic differentiation gene signature and are stalled in their differentiation capacity. We found that inducing autophagy, which is reduced in DMD progenitors, led to enhanced differentiation. Our findings provide molecular evidence of satellite cell dysfunction in DMD and suggest pathways to target and enhance their regenerative capacity.

## Introduction

Satellite cells, which are muscle-resident stem cells, are responsible for postnatal muscle growth, maintenance of muscle homeostasis, and muscle repair in response to damage caused by exercise and injury[1]. Satellite cells are named for their distinct anatomical location, as they typically reside in a quiescent state adjacent to the myofiber situated between the surrounding basal lamina and the sarcolemma membrane[2]. Upon a regeneration-inducing stimulus, satellite cells activate and undergo myogenic commitment, transitioning into a transient-amplifying population of proliferative myogenic progenitors (known as myoblasts), and subsequently terminally differentiate into myocytes that undergo fusion to help repair damaged myofibers[3].

Regenerative myogenesis is thus critically dependent on the regenerative capacity of satellite cells[4,5,6]. Distinct stages of cell fate during myogenesis are well characterized and can be inferred by the expression of specific genes as they progress through the myogenic program. Quiescent satellite stem cells express high levels of the paired-box transcription factor *Pax7* and quiescence-associated genes such as *Cd34*, *Calcr*, and *Spry1*[7,8,9,10]. Those that have become committed to the myogenic program express the myogenic commitment factor *Myf5*[11]. Proliferating myoblasts express high levels of *Myod1* and begin to downregulate *Pax7*[12]. Differentiating myocytes express *Myog*, followed by expression of *Mymk* and *Mymx* to aid in fusion to damaged myofibers, while *Myf6* and myosin heavy chain isoforms are expressed by mature myofibers[13,14,15,16].

While the myogenic process represents a mostly linear trajectory, multiple lines of evidence support the notion that the satellite cell population is heterogenous with respect to their propensity for self-renewal and differentiation potential[17,18,19]. Satellite cell heterogeneity has been described both at the molecular

and functional level. At the pinnacle of the hierarchy, satellite cells with enhanced self-renewal capacity that maintain the satellite stem cell pool have high levels of *Pax7* and *Cd34*, do not express *Myf5*, are slow cycling and retain parental template DNA strands[8,11,20,21,22]. In contrast, satellite cells that are primed for differentiation have lower levels of *Pax7* and *Cd34*, express *Myf5*, are fast cycling, and inherit daughter DNA strands. When subjected to transplantation assays, the primed satellite cells preferentially undergo differentiation and fuse to contribute to myofibers, while the satellite stem cells have the additional ability to engraft as satellite cells and contribute to the stem cell reservoir.

Recent advancement of single cell transcriptomic technologies has allowed for the characterization of satellite cell populations from resting and regenerating muscle. Initial single cell RNA-sequencing (scRNA-seq) of prospectively isolated satellite cells compared single cell transcriptomes of 21 satellite cells, which indicated transcriptional heterogeneity[23]. Current methods allow for efficient sequencing in the magnitude of several thousand prospectively isolated satellite cells, or a few hundred satellite cells from whole muscle tissue preparations. These studies have not only confirmed the heterogenous nature of the satellite cell population and the known myogenic trajectory of satellite cells following injury but have also revealed distinct gene expression signatures that occur as a result of tissue dissociation procedures[24,25,26,27,28]. Additionally, we now have information pertaining to the impact of aging and muscle degenerative diseases on satellite cell heterogeneity and transcriptional changes at the single cell level[29,30,31,32,33,34].

Due to the critical role of satellite cells in muscle repair and the potential for harnessing their regenerative capacity for therapies, the role of satellite cells in myopathies is an area of intense investigation. Muscular dystrophies are a heterogenous group of genetic muscle degenerative disorders characterized by progressive muscle wasting[35]. Duchenne muscular dystrophy (DMD), which impacts one in every 5,000 male births worldwide, represents the most prevalent form of muscular dystrophy[36]. Progressive muscle wasting renders boys with DMD wheelchair-dependent by the age of 15 and limits life expectancy to between 20-30 years. While treatments have been developed that have prolonged the lifespan of patients, there is still no cure. DMD is caused by mutations in the X-linked *DMD* gene, which is the largest known human gene with 79 exons, spanning over 2,300 kb[37]. Mutations that lead to loss of expression of the protein product dystrophin result in DMD, while partial expression of dystrophin results in the milder Becker muscular dystrophy[35]. The vast heterogeneity of DMD mutations, the large size of the *DMD* gene, and the inefficient transduction of muscle tissue and muscle stem cells, have impeded therapeutic development resulting in a critical need for a cure for this lethal disease.

In healthy muscle, the 427 kDa dystrophin protein is an integral component of the dystrophin glycoprotein complex (DGC), a large multimeric protein complex that spans the myofiber membrane playing a critical role in its integrity and stability[38,39,40]. The absence of dystrophin in DMD results in the loss of a functional DGC and reduced expression of several DGC components, thus rendering the myofibers susceptible to contraction-induced damage[41]. In addition to being expressed in the myofiber, dystrophin is also expressed in satellite cells, where it mediates the establishment of cell polarity to enable asymmetric stem cell division[42]. Accumulating evidence supports the notion that dystrophin-deficient satellite cells exhibit intrinsic dysfunction which leads to impaired regenerative capacity[43,44,45]. However, whether satellite cells are directly impacted by dystrophin loss or indirectly affected due to the chronic degenerative niche, and the extent to which satellite cell dysfunction contributes to DMD pathology, has yet to be resolved. In addition, whether dystrophin-deficient satellite cells are fully capable to undergo regenerative myogenesis and successfully contribute to muscle repair is still unclear.

To address these questions, we focused on satellite cells from two mouse models of DMD. The *mdx* mouse, which has a C57BL/10 genetic background, is the most widely used experimental mouse model of DMD[46]. However, despite harboring a naturally occurring null mutation in the *Dmd* gene, these mice exhibit mild dystrophy phenotypes and a minimal reduction in lifespan. While *mdx* mice do not fully recapitulate the human disease, these mice are well characterized and have provided useful insight into the contribution of satellite cells in DMD. In contrast, D2-*mdx* mice, which are *mdx* mice with a DBA/2 genetic background, exhibit a severe dystrophic pathology and a reduced lifespan of 12-18 months[47,48]. The differences between the *mdx* and D2-*mdx* models are attributed to a polymorphism in the latent TGF-β-binding protein 4 gene (*Ltbp4*) in the DBA/2 genetic background, leading to enhanced TGF-β signaling and fibrosis. Thus, we sought to establish how loss of dystrophin impacts satellite cells in both moderate and severe mouse models of DMD. By using both the *mdx* and D2-*mdx* models, we aimed to determine cell type intrinsic impairments due to dystrophin-deficiency and evaluate the contribution of the degenerative niche on satellite cell dysfunction. We employed scRNA-seq to assess the impact of dystrophin-deficiency on the satellite cell transcriptome and satellite cell heterogeneity. While both single cell and single nucleus sequencing have been performed using various DMD rodent models, these studies were performed on whole muscle tissue where satellite cell coverage was limited[31,32,49]. Thus, we performed our scRNA-seq analysis on prospectively isolated satellite cells from *mdx*, D2-*mdx*, and their respective wildtype counterparts.

In contrast to healthy satellite cells, which were mostly quiescent or stress-activated due to the isolation procedure, DMD satellite cells were skewed towards myogenic progenitor populations that have advanced farther along the myogenic program. Differential gene expression analyses revealed distinct impairments in satellite cells (upregulation of programmed cell death) and myogenic progenitors (upregulation of cellular senescence). Our scRNA-seq data revealed a DMD-associated satellite cell cluster that is unique to *mdx* and D2-*mdx* satellite cells that suggest an alternative, stalled differentiation fate. These cells express high levels of the cell cycle inhibitor *Cdkn1c* and exhibit an impaired differentiation gene signature. Interestingly, the majority of differentially expressed genes and enriched gene ontology (GO) processes between the satellite cells of each DMD model and their respective controls overlapped between the two DMD models. To address if DMD satellite cells exhibit impaired myogenic differentiation, we performed *in vivo* injury experiments and assessed gene expression and satellite cell dynamics. Activation of DMD satellite cells within a dystrophic niche revealed distinct differences in myogenic regenerative capacity. Finally, to counteract the increased senescence, we asked if modulating the nutrient recycling autophagy pathway, which is known to prevent senescence, could increase the regenerative potential of DMD satellite cells[50]. We found that autophagy is downregulated in DMD myogenic progenitors and that inducing autophagy with the autophagy promoting Beclin 1 peptide improved their differentiation and thus capacity for regeneration. Our findings indicate that DMD satellite cells exhibit intrinsic dysfunction that is specific to loss of dystrophin that is not simply a consequence of the severity of the dystrophic niche. Importantly, correcting these satellite cell dysfunctions has the potential to improve regenerative capacity, which is a critical step forward for addressing muscle repair deficits in muscle degenerative diseases.

## Results

### Altered muscle regeneration and satellite cell profiles in *mdx* and D2-*mdx* mice

To characterize the muscle tissue and the muscle-resident satellite cells in mild and severe DMD mouse models, we isolated tibialis anterior (TA) muscles from three-month-old *mdx* and D2-*mdx* mice, along with their respective wildtype counterparts C57BL/10ScSn (B10) and DBA/2 (DBA). As expected, hematoxylin and eosin staining of TA cross-sections from *mdx* and D2-*mdx* mice revealed signs of

chronic muscle degeneration (Figure 1A). We observed the presence of centrally nucleated myofibers, indicative of muscle regeneration, in both *mdx* and D2-*mdx* muscles, which were not present in wildtype muscles. Analysis of myofiber cross-sectional area across whole TA sections revealed increased variability in the myofiber size of dystrophic muscles compared to wildtype controls, a common feature of DMD (Figure 1B). *Mdx* and D2-*mdx* myofibers were on average larger, indicating hypertrophy, while D2-*mdx* myofibers also skewed towards having a higher proportion of small fibers compared to *mdx* (Figures 1B and S1A). There was no difference in the shape of dystrophic myofibers compared to wildtype (Figure S1B).

To characterize muscle regeneration in these dystrophic mouse models, we performed immunostaining for embryonic myosin heavy chain (eMHC) on TA cross-sections to visualize regenerating myofibers and the canonical satellite cell marker PAX7 to determine satellite cell content. While wildtype muscles exhibited little to no eMHC+ myofibers, dystrophic muscles exhibited a significant increase in the percentage of eMHC+ myofibers (Figure 1C-D). Moreover, the percentage of eMHC+ myofibers was greater in *mdx* compared to D2-*mdx*, indicating an increased presence of regenerating fibers in three-month-old *mdx* mice. As previously reported, we found that *mdx* mice have an increased number of PAX7+ satellite cells per $mm^2$ compared to B10 controls[51,52] (Figure 1E-F). In contrast, D2-*mdx* mice exhibited significantly lower numbers of PAX7+ satellite cells per $mm^2$ compared to DBA controls. Thus, *mdx* muscles exhibit persistent regeneration and enhanced satellite cell numbers, while D2-*mdx* muscles, despite also showing increased regeneration, have reduced satellite cell content compared to their wildtype counterpart.

In addition, we isolated single myofibers from extensor digitorum longus (EDL) muscles to assess satellite cell and myogenic progenitor content. Freshly isolated myofibers were immediately fixed and immunostained for the satellite cell marker PAX7 and the myogenic differentiation marker MYOG. Consistent with our satellite cell quantification from TA cross-sections, *mdx* EDL myofibers have the highest numbers of PAX7+ cells, indicating increased satellite cell content compared to B10 and DBA controls (Figure 1G-H). In contrast, we did not observe a difference in satellite cell content in D2-*mdx* EDL myofibers compared to DBA control. Moreover, both dystrophic models exhibited an increase in the number of MYOG+ differentiating cells, which are virtually absent in myofibers isolated from resting wildtype muscle (Figure 1I).

**Single cell transcriptomic profiling reveals differences in satellite cell heterogeneity within healthy and dystrophic muscle**

We observed differences in the muscle regeneration and satellite cell profiles between two different dystrophin-deficient DMD mouse models. Previous studies indicate that satellite cells in DMD have impaired asymmetric cell division and myogenic commitment[42,43]. We therefore asked how does the loss of dystrophin impact DMD satellite cells? To focus on the impact of dystrophin deficiency on satellite cell function and heterogeneity, we performed scRNA-seq on prospectively isolated satellite cells (Figure S2A). Satellite cells were isolated from the hindlimb muscles of *mdx* and D2-*mdx* mice, along with their wild-type counterparts B10 and DBA, by fluorescence-activated cell sorting (FACS)[53].

We captured and subjected 5,448 cells from B10; 6,781 cells from *mdx*; 3,373 cells from DBA; and 6,058 cells from D2-*mdx* to single cell transcriptomic sequencing. Following quality control and doublet removal, sequences from the four individual libraries were integrated and cell clustering was performed and visualized using uniform manifold approximation projection (UMAP) (Figure S2B-C). Cell clusters were identified by examining highly expressed genes unique to each cluster and comparing these with published scRNA-seq data sets from satellite cells and whole muscle[25,26,27,28] (Figure S2D). While the majority of our isolated cell population were satellite cells and myogenic

progenitors (72.48 - 96.47% of total cells), we also detected the presence of pericyte, vascular smooth muscle (VSM), glial, Schwann, white blood (WBC), and endothelial cells (Figure S2E-F).

Removal of non-myogenic cell types resulted in 4,487 cells from B10; 4,885 cells from *mdx*; 2,740 cells from DBA; and 4,183 cells from D2-*mdx* remaining, comprised of a combination of satellite cells and myogenic progenitors. Sub-clustering of these myogenic cells at a resolution of 0.2 resulted in the identification of eight transcriptionally distinct clusters (Figure S3A-B). Based on their gene expression signature, we designated these clusters as quiescent muscle stem cell (MuSC), early activated MuSC 1, early activated MuSC 2, cycling progenitors, differentiating myocytes, a population comprised mainly of dystrophic satellite cells (which we termed DMD enriched), immunomyoblasts, and myonuclei (Figure S3C). The mature myonuclei, which express high levels of mature muscle genes *Acta1*, *Tnnc2*, *Tnnt3*, represented a minor portion of total myogenic cells (0.04 - 0.11%). To focus on satellite cell and myogenic progenitor populations, we removed this myonuclei population from our downstream analyses.

UMAP analysis of integrated satellite and myogenic progenitor cells from the four different strains using the "find neighbors" algorithm allowed visualization of the seven distinct cell clusters, where cells with similar gene expression within each strain were mapped together (Figure 2A). Using the same resolution parameters, a UMAP analysis was performed without "find neighbors" (Figure 2B). In this case, cells from the same cluster in different strains were not mapped together, and instead, cells clearly mapped by strain (Figure 2C). These UMAPs provided two distinct ways to visualize the data, one in which cells from different strains are integrated and grouped by cluster (Figure 2A) and one in which cells are grouped by strain (Figure 2B).

As expected from satellite cells isolated from healthy and homeostatic resting muscle (B10 and DBA), the majority of wildtype satellite cells were found within the quiescent MuSC and early activated MuSC clusters (93.84% in B10 and 94.01% in DBA), which express high levels of *Pax7* and *Myf5* (Figure 2D-F). Cells within the quiescent MuSC cluster express high levels of genes associated with satellite cell quiescence (*Cd34, Notch3, Hes1*) (Figure 2D)[8,54,55]. The early activated MuSC clusters resembled quiescent satellite cells, but additionally expressed stress response genes (*Fos*, *Junb*, *Jund*) and genes associated with satellite cell activation (*Ccnd1*, *Sdc4*) caused by the tissue dissociation and FACS isolation procedure, which result in breaking quiesence[24].

Not surprisingly, we observed a shift in dystrophic satellite cells from quiescent and early activated states (63.07% in *mdx*; and 65.70% in D2-*mdx*) towards myogenic progenitor states (Figure 2E-F). These myogenic progenitor clusters included a cycling progenitor population that expresses cell cycle genes (*Cdk6*, *Mki67*) as well as the myogenic differentiation regulatory factor *Myod1*, and a differentiating myocyte population that expresses the late differentiation marker *Myog* (Figure 2D). Cell cycle analysis confirmed that the cycling progenitor population had the highest percentage of cells in G2/M and S phase (Figure S3D). Interestingly, a significant proportion of dystrophic cells were found in the DMD enriched cluster (20.83% *mdx*; and 15.03% D2-*mdx*) compared to their healthy counterparts (1.25% B10 and 1.46% DBA) (Figure 2E-F). These cells express a combination of quiescence and stress response genes, and uniquely express high levels of immunoglobulin superfamily containing leucine-rich repeat (*Islr*) and the cyclin dependent kinase inhibitor 1C (*Cdkn1c*) (Figure 2D). As previously reported, we noted a minor population of immunomyoblasts (0.22-2.45% in all four mouse strains) that are enriched in immune genes (*Ifit1*, *Ifit3*, *Isg15*) (Figure 2D-F)[26].

We utilized gene expression scores from published studies to validate our cell clusters (Figure S3E, Table S1). We examined the "genuine quiescence" and "primed core" expression signatures established

from bulk RNA-sequencing of *Cd34*$^{High}$ and *Cd34*$^{Low}$ satellite cells[8]. Additionally, we used "satellite cell", "myoblasts/myocytes", and "myonuclei" gene signatures recently generated from murine scRNA-seq data[56]. We also validated the early activated MuSC clusters using the "core stress signature" determined from tissue dissociation-induced transcriptomic changes[24] and the immunomyoblast cluster from an "immunomyoblast" score generated from scRNA-seq data of regenerating muscle[26].

Moreover, when we assessed the expression of these various scores across the different mouse strains, we confirmed that wildtype B10 and DBA cells are enriched for the "genuine quiescence" and "satellite cell" scores (Figure S3F). In contrast, dystrophic *mdx* and D2-*mdx* cells exhibit higher expression of the "myoblasts/myocytes", "primed core", and "core stress signature" scores compared to wildtype cells. Altogether, results from our scRNA-seq analysis of satellite cells isolated from two different DMD models revealed a skewing of cells towards progenitor populations in the absence of dystrophin, which reflects the chronic regeneration observed in dystrophic muscle. We also identified a population of "DMD enriched" cells that are distinct to dystrophic satellite cells and may represent a DMD-specific dysfunctional satellite cell population.

**Differential gene expression in DMD satellite cells reveal distinct dysfunctions between stem cells and progenitors**

Principal component analysis revealed that the most significant source of variation between the four data sets is between disease (DMD) and healthy cells suggesting that loss of *Dmd* expression is driving the most significant changes between samples and not differences between the genetic background of the two DMD models (Figure 3A). Dystrophin-deficiency in DMD is known to impact the expression of components within the dystrophin glycoprotein complex (DGC). Thus, we assessed the expression profile of DGC genes within our scRNA-seq data set. In agreement with studies demonstrating that *Dmd* is expressed in satellite cells[42,57], we confirm that the expression of *Dmd* seen in healthy B10 and DBA satellite cells is significantly reduced in dystrophic satellite cells (Figure 3B). We also confirm the expression of other DGC components in satellite cells including utrophin, dystroglycan, sarcoglycans, sarcospan and syntrophin. While most DGC genes were downregulated in dystrophic satellite cells, *Sntb2* was an exception to this trend and exhibited increased expression in dystrophic compared to healthy satellite cells (Figure 3B).

Global differential gene expression analysis between DMD vs healthy satellite cells revealed 1,147 differentially expressed genes between *mdx* and B10 (Figure 3C) and 1,642 differentially expressed genes between D2-*mdx* and DBA (Figure 3D). When assessing differences based on genetic background, we found 656 differentially expressed genes between D2-*mdx* and *mdx*, and 729 differentially expressed genes between DBA and B10 (Figure S4A-B). We found 742 upregulated genes in *mdx* vs B10 and 774 upregulated genes in D2-*mdx* vs DBA (Figure 3E). Interestingly, more than half of these genes (481 genes) are overlapping between the *mdx* and D2-*mdx* sets, suggesting that despite differences in disease severity between the two DMD models, the majority of differentially expressed genes due to dystrophin loss are common to both *mdx* and D2-*mdx*. Gene Ontology (GO) enrichment analysis of the upregulated genes in both *mdx* and D2-*mdx* revealed extracellular matrix, cytoskeleton in muscle cells, muscle structure development, and mitotic cell cycle as the top enriched biological processes and signaling pathways (Figure 3F-G). We observed 730 downregulated genes in *mdx* vs B10 and 868 downregulated genes in D2-*mdx* vs DBA, with 411 overlapping between the two comparisons (Figure 3H). GO enrichment analysis indicated neuron projection development and cell-cell adhesion as the top enriched downregulated pathways (Figure 3I-J).

In our comparison between the DBA and B10 backgrounds (Figure S4A-B), cell cycle pathways were upregulated specifically in D2-*mdx* vs *mdx* (Figure S4C-D). Skeletal muscle cell differentiation was downregulated specifically in DBA vs B10, while muscle tissue development was downregulated in both D2-*mdx* vs *mdx* and DBA vs B10 (Figure S4F-H). These results suggest that muscle regeneration pathways are upregulated in B10/*mdx* compared to DBA/D2-*mdx*, which reflect the observed reduction in muscle regeneration of young D2-*mdx* mice[58].

To focus on DMD-specific gene expression differences within different cell types we combined quiescent MuSC, early activated MuSC 1, and early activated MuSC 2 clusters together into what we termed the "satellite cell" group (Figure S5A). We then grouped cycling progenitors, differentiating myocytes, and DMD enriched clusters together into the "myoblast progenitor" group (Figure S5B). Differential gene expression analysis was performed between DMD and healthy satellite cells within these two groups of distinct myogenic stages. Our analysis revealed 337 differentially expressed upregulated genes in *mdx* vs B10 satellite cells and 335 genes in D2-*mdx* vs DBA, with 192 of these genes overlapping between *mdx* and D2-*mdx* comparisons (Figure 4A-B). In myogenic progenitors, we found 262 upregulated genes in *mdx* vs B10 and 285 upregulated genes in D2-*mdx* vs DBA, with 150 of these genes overlapping (Figure 4C-D).

Interestingly, we observe differential GO enrichment of distinct biological pathways between DMD satellite stem cells and myoblast progenitors, indicating unique dysfunctions between different myogenic states. In both *mdx* and D2-*mdx* satellite stem cells, the regulation of programmed cell death (apoptosis) was highly enriched (Figure 4B). Interestingly, negative regulation of cell differentiation was also observed in DMD vs healthy satellite cells. In contrast, in *mdx* and D2-*mdx* myoblast progenitors, cellular senescence was amongst the top enriched GO terms (Figure 4D). Muscle cell differentiation, cell-substrate adhesion, and cell proliferation were common enriched pathways in both satellite cells and myogenic progenitors in DMD cells (Figure S5C-D).

To examine if DMD satellite cells are indeed undergoing cell death by apoptosis, we performed terminal deoxynucleotidyl transferase dUTP nick-end labeling (TUNEL) on freshly isolated EDL myofibers from B10 and *mdx* mice (Figure S5E). In agreement with our scRNA-seq data (Figure 4B), we observed the presence of TUNEL+ satellite cells in *mdx* myofibers (Figures 4E). *Mdx* myofibers have more satellite cells compared to control fibers and we found that 15% of these were TUNEL+ (Figure 4F), indicating double stranded DNA breaks, a hallmark of apoptosis. In contrast, we did not observe any TUNEL+ satellite cells in control B10 fibers.

Our GO enrichment analysis of DMD myogenic progenitors revealed increased senescence, which has been reported in DMD muscles (Figure 4D)[31,44,59]. We assessed the expression of senescence genes *Cdkn1a* ($p21^{Cip1}$), *Cdkn2a* ($p16^{Ink4a}$), and *Cdkn2b* ($p15^{Ink4b}$) in our scRNA-seq data set and confirmed increased expression and percentage of cells expressing senescence genes in DMD satellite cells compared to healthy controls (Figure 4G). We validated this by performing droplet digital PCR (ddPCR) for senescence genes from freshly isolated satellite cells from B10, *mdx*, DBA, and D2-*mdx* mice and confirmed increased expression of *Cdkn1a* and *Cdkn2a* in both *mdx* and D2-*mdx* compared to wildtype controls (Figure 4H). We also performed senescence-associated β-galactosidase (SA-β-Gal) staining in TA cross sections from B10, *mdx*, DBA and D2-*mdx* mice (Figure 4I). Quantification of SA-β-Gal+ nuclei revealed significantly increased numbers of senescent nuclei per $mm^2$ of tissue in DMD muscles compared to wildtype controls (Figure 4J).

**Identification of an impaired myogenic differentiation gene signature of in dystrophic satellite cells**

Dystrophic satellite cells were skewed towards myogenic progenitor clusters (cycling progenitors, differentiating myocytes and DMD enriched) (Figure 2E-F). When assessing the expression of established "genuine quiescence" and "primed core" gene signatures in our scRNA-seq data, wild type B10 and DBA satellite cells were enriched for the genuine quiescence signature[8] (Figure 5A). In contrast, *mdx* and D2-*mdx* satellite cells exhibited higher expression of the primed core signature (Figure 5B). In addition, our GO-term enrichment analyses revealed that muscle cell differentiation and muscle structure development GO terms were enriched in DMD vs healthy satellite cells and progenitors (Figure S5D), which included genes *Mef2c*, *Myog*, *Myof*, *Cdh2*, and *Igf2*. Thus, we asked if DMD satellite cells are more differentiated compared to wildtype cells due to being chronically activated within a dystrophic muscle niche or if their abnormal expression of myogenic genes represent a state of impaired differentiation?

We interrogated our scRNA-seq data and assessed expression levels of canonical satellite cell and myogenic differentiation markers (*Pax7*, *Myf5*, *Myod1*, and *Myog*). *Pax7* and *Myf5* levels were highest in B10 and DBA cells and reduced in *mdx* and D2-*mdx* (Figure 5C). In contrast, *Myod1* and *Myog* levels were higher in *mdx* and D2-*mdx* compared to wildtype controls. These results were validated by ddPCR analysis of freshly isolated satellite cells from B10, *mdx*, DBA, and D2-*mdx* mice (Figure 5D). The reduced expression of satellite stem cell markers (*Pax7* and *Myf5*) and increased expression of myogenic differentiation markers (*Myod1* and *Myog*) would suggest that DMD satellite cells exist in a more differentiated state. However, when we examined the expression of genes involved in regulating myogenic differentiation, we found that DMD satellite cells express higher levels of anti-differentiation genes (*Id3*, *Runx1*, *Jdp2*) and lower levels of pro-differentiation genes (*Igfbp5*, *Meg3*, *Megf10*) compared to their wildtype counterparts (Figure 5E). This suggests an impairment of the normal myogenic program in DMD satellite cells.

To infer myogenic differentiation trajectories, we performed pseudotime analyses using the Monocle 3 package. Using the expression of *Cd34* as an anchor point marking genuine quiescence, we set the root of the trajectory in the quiescent MuSC cluster[8] (Figure 5F). The pseudotime analysis revealed two main trajectories, each with a branch point resulting in four possible end points, which represent distinct cell fates (Figure 5G-H). The main trajectory goes from quiescent cells towards cycling progenitors and represents the furthest pseudotime point from quiescence (Figure 5G-H). Within this trajectory, we observe a branch going toward the early activated MuSC. The second main trajectory goes from quiescence directly to differentiating myocytes or branches to the DMD enriched cluster. Visualization of these pseudotime trajectories on the UMAP for each mouse strain (Figure 5I) revealed that B10 and DBA cells could be found in three of these cell fates, with the majority of cells found in the early activated MuSC 2 fate, and few cells in cycling progenitor and differentiating myocyte fates. In contrast, *mdx* and D2-*mdx* cells were clearly skewed towards the DMD enriched fate, with some cells also found in the differentiating myocytes and cycling progenitor fates. These results suggest that DMD satellite cells exhibit an altered fate, which led us to interrogate if this represents an impaired differentiate state.

**DMD satellite cells exhibit impaired *in vivo* regenerative myogenesis**

Genes that are highly expressed and unique to the DMD enriched cluster include several genes that have been associated with DMD (*Col1a1*, *Col1a2*, *Islr*, *Mest*, *S100a11*, *Postn*)[60,61,62,63]. In addition to these genes, cells in this cluster also have increased expression of the negative cell cycle regulator *Cdkn1c* ($p57^{Kip2}$), which has not previously been associated with DMD (Figure 6A). *Cdkn1c* expression is induced in activated and proliferating myoblasts and coordinates the switch between proliferation and cell-cycle arrest in differentiating progenitors[64]. We validated the increased expression of *Cdkn1c* in dystrophic satellite cells by ddPCR (Figure 6B). Increased expression of *Cdkn1c* would suggest that

DMD satellite cells within this cluster are non-proliferating and stalled in their ability to undergo differentiation. Indeed, the DMD enriched cluster exhibits low *Pax7* expression and also lower *Myod1* and *Myog* in comparison to the differentiating myocyte cluster (Figure 2D, S6A), indicating that they are not simply cells undergoing a normal transition from a proliferative state.

To assess the differentiation potential of DMD satellite cells we utilized an *in vivo* muscle regeneration approach to induce differentiation within the context of a dystrophic niche. We performed intramuscular injury on the TA and gastrocnemius muscles of B10 and *mdx* mice and then prospectively isolated satellite cells from these mice at one- and three-days post injury (1 and 3 DPI). Gene expression analyses by ddPCR from these samples were compared to satellite cells isolated from non-injured (NI) muscles. Gene expression profiles from B10 satellite cells followed the expected trends of satellite cells transitioning from quiescence (NI) to activation (1 DPI) and proliferation (3 DPI). Expression of markers of quiescence (*Cd34*, *Calcr*) as well as satellite stem cells (*Pax7*, *Myf5*) were highest in NI cells and the expression of these genes were reduced upon activation (Figure 6C, S6B). *Myod1* expression was highest in B10 1 DPI activated cells, while *Myog* levels increased from 1 to 3 DPI. Interestingly, when we examined the gene expression profile of *mdx* satellite cells following injury, we did not observe the expected upregulation of *Myod1* at 1 DPI (Figure 6C). In contrast, *Myog* levels were elevated in *mdx* cells compared to B10 at all time points. Moreover, proliferation markers *mKi67* and *Pcna* were significantly reduced at 1 DPI in *mdx* cells compared to B10 control (Figure S6C).

While ddPCR provides a quantitative readout for gene expression, gene expression does not always correlate with protein expression or represent actual numbers of cells expressing a given gene. Thus, we also assessed the protein expression and the number of satellite cells and myogenic progenitors using the gold standard *ex vivo* myofiber approach. Rather than isolating the myofibers and subsequently culturing them *ex vivo*, we took the approach of performing intramuscular injury on the TA muscle and then collecting the adjacent EDL muscle at five-, seven-, and nine-days post injury (5, 7, and 9 DPI) to examine satellite cell differentiation that was induced *in vivo*. These *in vivo* injured myofibers were immunostained for PAX7 and MYOG (Figure 6D). Quantification of myogenic cells on B10 injured myofibers revealed an expected increase in the number of MYOG+ cells from 5 to 9 DPI (Figure 6E). In contrast, we did not observe an increase in MYOG+ cells in *mdx* injured fibers and the number of MYOG+ cells were significantly reduced in *mdx* fibers at 9 DPI. The number of PAX7+ cells per fiber was increased over all time points in *mdx* compared to B10 injured fibers. When representing the data as a ratio of MYOG+ to PAX7+ cells, *mdx* myofibers have significantly reduced MYOG+/PAX7+ ratios at 7 and 9 DPI. Most strikingly, we observed the presence of large clusters of cells in *mdx* fibers (Figure 6F) at all time points that were virtually absent in B10 fibers except for at 9 DPI (Figure 6G, S6D). These cell clusters contained myogenic cells that included PAX7 and MYOG positive nuclei as well as the presence of $p57^{Kip2}$ (*Cdkn1c*) positive cells (Figure 6F). The numbers of large cell clusters (>1000um$^2$) as well as the area of the observed cell clusters were increased in *mdx* injured myofibers compared to B10 controls (Figure 6G). Altogether, our scRNA-seq data along with our *in vivo* regenerative myogenesis analyses of DMD satellite cells indicate that DMD satellite cells exhibit impaired myogenic differentiation.

**Altered senescence and autophagy dynamics in DMD satellite cells**

Cellular senescence was enriched in the DMD myoblast progenitor group compared to wildtype progenitors. We used a gene list derived from the senescence GO term (GO: 0090398) to generate a 'senescence GO' score (Table S1). Using this score, we confirmed that senescence is highest in the DMD enriched and differentiating myocyte clusters (Figure 7A). The presence of senescent cells within the differentiating myocyte cluster confirms recent work indicating that healthy satellite cells transition

into transient senescence-like state during the regenerative process[29,65]. We assessed the expression of senescence associated genes *Cdkn1a* and *Cdkn2a* in satellite cells following injury by ddPCR and found that in B10 satellite cells, senescence genes increase upon activation (Figure 7B). These results suggest that expression of these senescence genes at certain time points during the regenerative program is normal and perhaps necessary. In contrast, DMD satellite cells exhibit significantly higher baseline senescence gene expression in non-injured satellite cells and exhibit impaired senescence dynamics during regeneration, thereby indicating a chronic persistence of senescence gene expression in DMD satellite cells (Figure 7B).

We hypothesized that the enhanced senescence is impairing the regenerative capacity of DMD satellite cells. In healthy quiescent satellite cells, cellular autophagy, a nutrient recycling pathway, has been shown to prevent senescence and thus maintain stemness and regenerative capacity[50]. To examine if cellular autophagy is dysregulated in DMD satellite cells we performed ddPCR analysis to assess the expression of a panel of autophagy genes (*Atg9a*, *Atg14*, *Map1lc3b*). Expression of autophagy genes were all downregulated in DMD satellite cells compared to wildtype controls (Figure 7C). Next, we assessed the expression of autophagy genes (*Atg9a*, *Atg14*, *Map1lc3b*, *Sqstm1*, and *Gabarap*) during injury-induced myogenesis. In wildtype satellite cells, expression of autophagy genes was highest during quiescence and reduced upon activation (Figure 7D). This trend was opposite of what we observed with respect to expression of senescence genes following injury. Moreover, dystrophic *mdx* satellite cells exhibit reduced autophagy in quiescence and activated (1 DPI) time points compared to B10 controls.

We used a published autophagy gene score[50] and the senescence GO score to assess the autophagy and senescence status within DMD and healthy satellite cell and myogenic progenitor groups from our scRNA-seq analysis. As expected, senescence was higher in DMD compared to healthy cells and there were increased numbers of cells expressing the senescence GO score in dystrophic myogenic progenitors compared to satellite cells (Figure S7A). In contrast, expression of the autophagy score was higher in dystrophic satellite cells but reduced in dystrophic myogenic progenitors. To determine if the autophagy and senescence scores were being expressed in distinct cells, we overlaid the two scores and determined correlation coefficients. There was minimal overlap between the expression of autophagy and senescence scores in all cell clusters from each mouse strain (Figure S7B). Thus, our data indicates that autophagy and senescence are mutually exclusive pathways during regenerative myogenesis in both DMD and wildtype satellite cells.

We asked if modulating autophagy would improve the differentiation capacity of DMD satellite cells. To address this, we used 3-methyladenine (3MA), a class III phosphoinositide kinase inhibitor that inhibits autophagy, and Tat-Beclin 1 (D11), an autophagy promoting peptide that contains 11 amino acids from the autophagy inducing protein Beclin 1[66,67]. We treated *mdx* primary myogenic progenitors with either 3MA or D11 and assessed their differentiation capacity (Figure 7E). While inhibiting autophagy with 3MA did not have a significant impact on differentiation, inducing autophagy with D11 resulted in enhanced differentiation of DMD progenitors (Figure 7F). Thus, inducing autophagy in DMD progenitors improves the differentiation capacity of DMD progenitors cells. Altogether, our results support the notion that counteracting these DMD progenitor-specific impairments (ie. enhanced senescence and reduced autophagy) can improve their endogenous regenerative capacity.

## Discussion

Single cell sequencing technologies have provided the ability to parse out cellular heterogeneity and identify transcriptomic differences within complex cell populations. Here, we used scRNA-sequencing

to elucidate the mechanisms by which satellite cells in DMD in particular are impacted by loss of dystrophin. Recent studies have used both single cell and single nucleus transcriptomic approaches to assess whole muscle tissue from various mouse and rat DMD models[31,32,49,68]. While these approaches have identified significant alterations in tissue-wide cellular diversity in DMD, our study uniquely focused on sequencing of the satellite cell population to gain sufficient sequencing depth to identify distinct satellite cell populations within the heterogenous satellite cell pool. By adequately capturing these subpopulations, we were able to elucidate molecular pathways that differ between DMD and healthy satellite cells and myogenic progenitors.

We aimed to address a long-standing question of whether or not satellite cells in DMD are intrinsically affected by dystrophin loss or if their dysfunction is due to the degenerative niche environment. To do so, we compared satellite cells from two DMD mouse models, the widely used *mdx* mouse and the more recent D2-*mdx* mouse. Of note, *mdx* and D2-*mdx* mice exhibit differences in satellite cell content. While *mdx* muscles have higher satellite cell numbers compared to their control counterpart, as previously shown[51,52], D2-*mdx* mice have reduced satellite cell numbers compared to DBA controls (Figure 1F). The lower satellite cell content in D2-*mdx* mice would support previous studies demonstrating that satellite cells have reduced regenerative capacity in DBA/2 muscles compared to C57BL/6, thereby impacting their ability to maintain a sufficient satellite cell pool to support regeneration within the context of chronic degeneration[47]. The altered muscle regenerative potential in DBA and D2-*mdx* is supported by our GO term enrichment analyses, which indicated reduced muscle tissue development and skeletal muscle differentiation when comparing satellite cells from the DBA versus B10 background (Figure S4G). Whereas an increase in satellite cell numbers have been reported in human DMD tissue[51], these differences in satellite cell number and muscle regeneration should be considered when utilizing the D2-*mdx* model.

Despite differences in disease severity between the *mdx* and D2-*mdx* DMD models, our analysis revealed that the majority of differentially expressed genes between DMD and healthy satellite cells overlapped across both genetic backgrounds. Moreover, many of the non-overlapping genes were found within shared GO terms, indicating that satellite cells exhibit similar molecular dysfunctions regardless of their exposure to a mild or severe dystrophic niche (Figure 3G, J). When directly comparing the transcriptomes of *mdx* with D2-*mdx* satellite cells, we found that cell cycle GO terms were uniquely enriched in D2-*mdx* (Figure S4D), while synaptic signaling and plasticity were downregulated in D2-*mdx*, indicating enrichment in *mdx* (Figure S4G).

Our study sheds light on the unresolved question regarding the regenerative capacity of dystrophic satellite cells. Prior to the discovery that dystrophin is expressed in the muscle stem cell, it was generally thought that the loss of dystrophin had little to no impact on satellite cells and their progeny, the myogenic progenitors. Studies reported no difference in the differentiation capacity of dystrophic satellite cells, or even accelerated myogenic differentiation kinetics suggesting that DMD satellite cells are capable of undergoing differentiation[69,70]. We have also observed the differentiation of dystrophic myogenic progenitors *in vitro*, but we propose that *ex vivo* culturing of progenitors results in a cell selection process that favors cells capable of proliferating and surviving in culture. However, earlier studies also indicated a cell-autonomous impairment in dystrophic satellite cells that renders them functionally unable to participate in muscle repair[45,71]. We now know that dystrophin expression in satellite cells is critical for establishing cell polarity and that dystrophin deficiency results in inefficient asymmetric stem cell divisions and impaired epigenetic-mediated expression of myogenic commitment genes[42,43]. Subsequent studies have also supported the notion that satellite cells and myogenic progenitors in DMD exhibit impaired function[31,32,44,72]. In keeping with this, our scRNA-seq analysis identified a DMD enriched cell cluster that uniquely expresses genes associated with DMD and they

express high levels of the cell cycle inhibitor *Cdkn1c*. This cluster accounted for 20.83% of *mdx* satellite cells (compared to 1.25% of B10) and 15.03% of D2-*mdx* satellite cells (compared to 1.46% of DBA) (Figures 2E-F). While *Cdkn1c* has been shown to be expressed in healthy satellite cells to facilitate the transition of proliferating progenitors to differentiated myocytes, we found that this cluster of cells expresses higher levels of stem cell markers *Pax7* and *Myf5* and lower levels of differentiation markers *Myod1* and *Myog* compared to the progenitor and myocyte clusters[64]. In addition, pseudotime analyses of our scRNA-seq dataset indicates that the DMD enriched cluster represents a distinct cell fate from the conventional myogenic trajectory (Figure 5G). Altogether, these results suggest that this DMD enriched cluster represents a stalled differentiation cell fate, unique to dystrophic satellite cells.

Gene expression analysis of pseudobulk satellite cell populations indicate reduced *Pax7* and increased *Myog* expression in DMD satellite cells (Figure 5C-D), suggesting that DMD satellite cells are less stem-like and are further along the myogenic lineage. While DMD satellite cells are skewed towards progenitor populations (Figure 2E), we propose that at least a subpopulation of dystrophic satellite cells is stalled in differentiation and exhibit dysregulated myogenic capacity. In line with this, less than 50% of DMD satellite cells are expressing the "primed core"[8] and "myoblast/myocyte"[56] scores (Figure S3F). To test this hypothesis, we used *in vivo* regeneration assays by inducing intramuscular injury and examined the regenerative capacity of DMD satellite cells. Our experiments revealed an impairment in regenerative myogenesis in *mdx* satellite cells compared to B10 controls (Figure 6C-G). Interestingly, while *mdx* satellite cells express lower levels of *Pax7* transcripts and higher levels of *Myog* transcripts, we show that the level of gene expression does not correlate with cell number as we observe increased PAX7+ cells and reduced MYOG+ cells in *mdx* fibers following injury. Our interpretation of these findings is that gene expression analysis of bulk cell populations does not provide information regarding the number of transcripts expressed per cell. Specifically, we propose that a few *mdx* cells may express a high level of *Myog* transcripts, while the majority of the population is MYOG-. Similarly, B10 control cells may express high levels of *Pax7* transcripts per cell resulting in a higher transcriptional output, but *mdx* cells have more cells expressing low levels of *Pax7* transcripts.

Surprisingly, we found large cell clusters uniquely in injured *mdx* myofibers (Figures 6F-G). As these myofibers were fixed immediately upon isolation and not cultured *ex vivo*, these cell clusters were formed *in vivo* and suggest an impairment in cell fusion. The presence of these *in vivo* myogenic clusters has not been described previously. Here, we show functional impairment of DMD satellite cells following the injury of dystrophic muscle. We attempted to characterize the nature of these clusters by immunolabeling with PAX7, MYOG, and $p57^{Kip2}$ (*Cdkn1c*) antibodies followed by confocal microscopy, however the large numbers and dense packing of these cells made it difficult to discern cell identities within clusters. Further experiments to isolate and characterize these cells by flow cytometry would provide important insight into this DMD enriched cell population.

An advantage to using scRNA-seq is the ability to evaluate if specific cell populations within different stages of the myogenic trajectory display differential gene expression signatures. Thus, we asked if more stem-like satellite cells exhibit unique DMD-induced dysfunctions compared to more differentiated myogenic progenitors. While several dysregulated molecular pathways were common between satellite cells and myogenic progenitors, including muscle cell differentiation and cell proliferation, we also observed enrichment of distinct pathways in each. We found that DMD satellite cells exhibit enrichment in programmed cell death and negative regulation of cell differentiation pathways (Figure 4B). In contrast, DMD myogenic progenitors exhibit enrichment in cellular senescence and DNA damage response pathways (Figure 4D). Recent studies have indicated that healthy myogenic cells transition through a transient senescent state during muscle regeneration and that senescent cells are a normal component within the regenerating muscle niche[29,34,65]. We also found

that control B10 satellite cells express increased levels of senescence-associated genes following injury that would confirm this trend (Figure 7B). In contrast to healthy satellite cells, DMD satellite cells exhibit altered dynamics of senescence and increased baseline expression of senescence-associated genes suggesting a chronic and dysregulated senescent state (Figure 7B). The chronic presence of these senescent cells would hinder muscle regeneration[34,59]. In line with this, we observed altered gene expression of myogenic factors during regeneration, supporting the idea that these cells are not progressing through the normal myogenic program (Figure 6C).

We also utilized scRNA-seq to interrogate pathways related to senescence, including the nutrient recycling macroautophagy pathway, which has previously been shown to be dysregulated in DMD muscle and satellite cells[73,74,75]. Our data supports this finding, showing that the dynamics of autophagy are dysregulated in dystrophic satellite cells. We found that the expression of autophagy genes is downregulated during healthy regenerative myogenesis (Figure 7D), while expression is universally lower in dystrophic satellite cells (Figure 7C-D). Interestingly, our scRNA-seq data indicate increased autophagy in satellite cells and reduced autophagy in myogenic progenitors (Figure S7A). Given the reciprocal relationship between autophagy and senescence, we overlaid autophagy[50] and senescence gene expression scores and found that cells expressing these pathways are mutually exclusive (Figure S7B). We propose that impaired senescence and autophagy dynamics impact the regenerative capacity of DMD satellite cells, given that the removal of senescent cells has been shown to be beneficial for muscle regeneration in healthy and disease contexts[30,31,34]. Indeed, we found that enhancing autophagy with Tat-Beclin D11, which induces autophagy independently of inhibiting the master metabolic regulator mammalian target of rapamycin, improved differentiation capacity of *mdx* progenitor cells (Figure 7E-F)[66]. Our results support earlier work indicating that autophagy reduction in DMD muscles correlates with reduced regenerative capacity and that inducing autophagy with agents such as rapamycin and the AMPK agonist AICAR can improve regeneration and pathology in *mdx* mice[73,76,77].

In conclusion, we provide molecular evidence that satellite cells are dysfunctional in DMD and that their reduced regenerative potential contributes to the characteristic progressive muscle wasting of the disease. The work described here serves as a critical resource characterizing the transcriptomes of two widely used DMD mouse models, *mdx* and D2-*mdx*, along with their wildtype counterparts. We also identify a unique DMD enriched satellite cell population, indicating a stalled differentiation state, and demonstrate that DMD satellite cells have increased apoptosis and altered senescence and autophagy dynamics. Our results indicate that DMD satellite cells are heterogenous with respect to their myogenic regenerative potential and their exhibition of impaired cellular pathways. We propose that gene therapies aimed at transducing satellite cells should examine the benefits and consequences of targeting specific satellite cell populations. Overall, our study provides a molecular map that illustrates how satellite cell subpopulations are impacted by the loss of dystrophin and will inform therapeutic strategies aimed at improving the regenerative capacity of DMD muscle.

## Methods

### Mice

Housing, husbandry and all experimental protocols for mice used in this study were performed in accordance with the guidelines established by the McGill University Animal Care Committee, which is based on the guidelines of the Canadian Council on Animal Care. C57BL/10ScSnJ (B10, #000476), C57BL/10ScSn-*Dmd*$^{mdx}$/J (mdx, #001801), DBA/2J (DBA2, #000671), and D2.B10-*Dmd*$^{mdx}$/J (D2-*mdx*, #013141) were purchased from The Jackson Laboratory. Two- to three-month-old male mice were used for all experiments.

**Muscle histology**
Cryostat cross-sections of tibialis anterior (TA) muscle of 10µm were used for hematoxylin and eosin (H&E) staining, senescence-associated β-galactosidase staining and immunofluorescent (IF) labelling.

Sections for H&E were fixed with 4% paraformaldehyde (PFA) and stained with Mayer's modified hematoxylin solution (Abcam) and washed for five minutes followed by differentiation with 1% HCl in 10% ethanol. Sections were stained with Eosin Y working solution (0.25% Eosin disodium salt (Sigma) in 80% ethanol with 0.5% glacial acetic acid), dehydrated and mounted with xylene mounting media (Fisher).

For PAX7 IF labelling, sections were fixed with 2% PFA for two minutes, followed by permeabilization for 15 minutes (0.1% triton X-100 + 0.1M Glycine in PBS) and blocking for one hour (5% donkey serum (DS) (Sigma) + 2% bovine serum albumin (BSA) + Mouse on Mouse Blocking Reagent (Vector Laboratories) in phosphate buffered saline (PBS)). Primary antibody incubation was done overnight at 4°C with pure PAX7 antibody with 5% DS + 2% BSA. Secondary incubation in labelling buffer (5% DS + 2% BSA in PBS) was done for one hour at room temperature, followed by Hoescht staining for 5 minutes. Slides were mounted with ProLong™ Gold antifade reagent (Thermo Fisher).

For MYOG and eMHC labelling, TA cryosections were fixed with 4% PFA for 10 minutes then permeabilized and blocked for one hour (0.1M glycine + 5% DS + 0.25% triton-X-100 in tris buffered saline (TBS)). Subsequently, cryosections were incubated overnight at 4ºC with primary antibody solution (1% DS + 0.25% triton-X-100 in TBS). Secondary antibody incubation and mounting were performed as above.

Sections were imaged using a Zeiss Axio Observer 7 at 20X, except for eMHC-stained cryosections which were imaged at an EVOS M5000 microscope using a 10X objective.

**Senescence-associated β-galactosidase staining**
Tibialis anterior (TA) sections were fixed for four minutes with 1% PFA and 0.2% Glutaraldehyde in PBS, followed by incubating for 30 minutes in PBS at pH 5.5. Sections were then incubated with X-gal staining solution (4mM potassium ferricyanide + 4mM potassium ferrocyanide + 2mM $MgCl_2$ +1 mg/mL X-gal and 0.04% IGEPAL (Sigma) in PBS at pH 5.5) for 48 hours at 37°C. Sections were subsequently washed in PBS for 10 minutes and fixed again with 1% PFA diluted in PBS for 10 minutes. Sections were counterstained with Hoescht. The stained sections were mounted with ProLong™ Gold antifade reagent and imaged using a Zeiss Axio Observer microscope.

**Single myofiber isolation**
Single myofibers were isolated from the extensor digitorum longus (EDL) muscle of mice (Brun 2018) that were either uninjured or mice that received injections of 1.2% $BaCl_2$ to the TA (30ul at 1.2%) five, seven or nine days prior to isolation to induce injury and thus activate satellite cells. After isolation, single myofibers were collected and fixed immediately in 2% PFA.

**IF and TUNEL staining on fibers**
Fixed myofibers were permeabilized for 10 minutes (0.1M glycine + 0.1% triton X-100 in PBS) then blocked for two hours (2% BSA + 2.5% DS + 2.5% goat serum (GS) in PBS). Primary antibody incubation was done overnight labelling solution (0.5% DS + 0.5% GS in PBS) at 4°C. Secondary antibody incubation was done for one hour at room temperature in labelling solution, followed by Hoescht staining for one minute. Fibers were mounted on slides with ProLong™ Gold antifade reagent.

TUNEL staining was done with the In Situ Cell Death Detection Kit (Roche). Fibers were fixed with 2% PFA, then permeabilized and blocked as previously described. Fibers were then incubated with TUNEL reaction mixture for one hour at 37°C followed by primary antibody incubation overnight at 4°C. Secondary antibody incubation, Hoescht and mounting on slides were performed as described above.

Myofibers were imaged using a Zeiss LSM710 with the exception of Figure 6D that was imaged at an EVOS M5000 microscope using a 20X objective.

**Quantification of IF images**

All image analysis was done with Fiji ImageJ[78]. PAX7+, MYOG+ and SA-Bgal+ nuclei quantification was performed using the cell counter feature. Cross sectional area of myofibers and aspect ratio was obtained using the automated muscle histology analysis algorithm Myosoft to define individual fiber ROIs via WGA staining[79]. Using this same software, the number of eMHC+ fibers were determined by automatically measuring mean grey value. These values were then corrected through background subtraction. A negative control was used to determine the range of values that represented "true" negatives and values above this (>75) were considered eMHC+.

**Satellite cell isolation**

Satellite cells were prospectively isolated from the hind limb muscles of mice as previously described[80]. Cells were labelled with negative and positive lineage markers (Table S2) and satellite cells were sorted using a BD FACSAriaTM III (BD Biosciences).

**Single cell RNA-sequencing and computational analyses**

For each mouse strain (B10, *mdx*, DBA, D2-*mdx*), ITGA7+/VCAM+/Lin- satellite cells from two mice were pooled, sorted and captured on the 10X Genomics Chromium platform and subjected to single cell transcriptomic sequencing. Following satellite cell isolation, the single-cell RNA-sequencing libraries were prepared using the 10X Genomics NextGen scRNA 3' V3.1 (10X Genomics, Pleasanton, CA) with approximately 10,000 satellite cells from each strain. Libraries were then sequenced with an Illumina NovaSeq6000 sequencer (Illumina, San Diego, CA). Reads were processed with Cell Ranger (version 3.0.1) and aligned to the mouse reference transcriptome mm10.

Computational analysis was performed using RStudio (version 4.2.1, 2022-06-23), and the data were imported with Seurat (version 5.1.0)[81]. Cells were filtered to remove cells with less than 1,000 or more than 5,000 genes, as well as cells with more than 8% mitochondrial genes, to eliminate low quality cells. Doublets were removed using DoubletFinder (version 2.0.4)[82]. After normalization and scaling, cells from the different mouse strains were integrated. The resolution was determined using the Clustree function (version 0.5.1) and unsupervised clustering was carried out using the FindClusters function[83]. The first clustering was done with a resolution of 0.1, and the sub-clustering of the myogenic cells was done with a resolution of 0.2. Differential gene expression and cluster identification were performed using FindAllMarkers function in Seurat. The scores were generated with the AddModuleScore function, using published genes lists. Stacked violin plots were made using the the StackedVlnPlot function[84]. Dot plots and feature plots were created using scCustomize package (version 2.1.2)[85]. Cell cycle analysis was done using the CellCycleScoring function of the Seurat Package.

**Principal component analysis (PCA) – Pseudobulk**

The processed individual datasets were merged, and the object was converted into a SingleCellExperiment object. Counts were aggregated with aggregateBioVar package (version 1.14.0)[86]. Differential gene expression was performed using DESeq2 Package (version 1.44.0)[87]. The PCA plot was generated using plotPCA function.

**Differential gene expression and Gene Ontology (GO) enrichment analysis**

Differentially expressed genes lists were generated using the FindMarkers function. Genes with Log2FC more than 1 and adj pVal less than 0.05 were selected for GO enrichment analysis. GO enrichment was performed using Metascape (metascape.org) with multiple gene lists using the Custom Analysis function[88]. GO Biological Processes, KEGG Pathway, Reactome Gene Sets, CORUM, WikiPathways, and PANTHER Pathway were selected. Terms with a p-value < 0.01, a minimum count of 3, and an enrichment factor > 1.5 were grouped into clusters based on their membership similarities. GO terms analysis has been performed with the enrichGO function of the clusterProfiler package version 4.12.0[89]. Volcano plots were generated using the EnhancedVolcano package (version 1.22.0)[90]. Venn Diagrams were generated using VennDiagram package (version 1.7.3)[91].

**Pseudotime analysis**

The pseudotime analysis was performed using Monocle3 package (version 1.3.7)[92]. The datasets were processed as described previously. The Seurat object has been transformed as a cell data set using the SeuratWrappers package (version 0.3.5). Cells were then clustered using the cluster_cells function. The trajectory was generated using the learn_graph function by adjusting the default setting of minimal_branch_len to 10, euclidean_distance_ratio to 1 and geodesic_distance_ratio to 1. Finally, cells were ordered along the learned trajectory.

**Droplet digital PCR (ddPCR)**

RNA was extracted from isolated satellite cells using the PicoPure RNA Isolation Kit (Applied Biosystems) and cDNA was generated with the SuperScript III First-Strand Synthesis System (Invitrogen). ddPCR was performed using ddPCR Supermix for Probes (no dUTP) (Biorad) and analyzed with the QX100 Droplet Digital PCR System (Biorad). A list of primers can be found in Table S3.

**Autophagy modulation assays**

Primary satellite cell-derived myoblasts were isolated from *mdx* mice as previously described[93]. Cells were seeded in proliferation media (20% FBS, 10% HS, 3% CEE, 10 ng/mL bFGF and 2 mM L-glutamine in Ham's F-10) on collagen-coated 35 mm plates. When cells reached 80-90% confluence, cells were treated for two hours with either 10 µM Tat-Beclin 1 D11 peptide (Novus Biologicals) or Tat-Beclin 1 L11S peptide scramble control (vehicle, Novus Biologicals); 5 mM 3-methyladenine (3-MA, Sigma) or water (vehicle)[66,67]. Following treatment, cells were induced to differentiate for two days in differentiation medium (50% DMEM, 50% F10, 5% HS). Cells were fixed and immunolabeled with MyHC antibody, and fusion index was determined as previously described[94].

**Statistical analysis**

For data not related to scRNA-seq, statistical analyses and visualizations were done in GraphPad Prism (version 10.2.2). Significance was determined through two-tailed unpaired t-tests, two-way analysis of variance (ANOVA) with Šídák's multiple comparisons test, mixed-effects analysis with Šídák's multiple comparisons test, or one-sided Fisher's exact test, as indicated. F and P values in figure legends for two-way ANOVAs and mixed-effects analysis describe row*column effect unless otherwise noted. Confidence interval = 95% for all tests.

Two-tailed t-tests in Figure 1 were performed on three biological replicates per group and df=4. For all two-tailed unpaired t-tests of strain comparison ddPCR data, n = 3 for all groups except D2-*mdx* where n = 4. For B10-*mdx* comparisons df=4, and for DBA-D2-*mdx* comparisons df = 5. For all two-way ANOVA tests, which were conducted on NI, 1 DPI and 3 DPI data, row factor (DPI) degrees of freedom (df) = 2 and column factor (strain) df = 1. Three biological replicates were used for all groups except B10 3DPI, where n = 4. Cluster data in Figure 6E and G was done using EDL fibers from one biological replicate per condition. Number of fibers counted are as follows: B10 - 5 DPI = 3, 7 DPI = 8, 9 DPI = 10; *mdx* – 5 DPI = 8, 7 DPI = 9 DPI = 11. Significance was then calculated via mixed-effects analysis due to uneven sample size. Row factor (DPI) df = 2 and column factor (strain) df = 1. β-galactosidase assays were done with three biological replicates per condition (df = 4) and significance calculated via two-tailed unpaired t-tests. TUNEL+ nuclei percentage was calculated from n = 25 B10 and n = 82 *mdx* PAX7+ nuclei from n = 8 fibers from B10 and n = 6 fibers from *mdx*. A one-sided Fisher's exact test was used as B10 has zero positives. Autophagy modulation assays were done on three biological replicates per condition (df = 4) and significance determined with two-tailed unpaired t-tests.

**Acknowledgements**
We thank Camille Stegen and Julien Leconte from the Flow Cytometry Facility, Frederique Dansereau and Giovanni Carrera-Viray from the Comparative Medicine and Animal Resources Centre, as well as Tony Kwan and Ashot Harutyunyan from the McGill Genome Centre. R.L.F. is the recipient of a Vanier Award (FRN: 186914). R.R. was a Muscular Dystrophy Canada Fellow. A.C. is the recipient of a Canada Graduate Scholarship - Master's award. S.L. is supported by the Défi-Canderel studentship from the Rosalind and Morris Goodman Cancer Institute and a Master's training scholarship from the Fonds de recherche du Québec - Santé. N.C.C. is the recipient of a Chercheur-boursier Junior 1 award from the Fonds de recherche du Québec - Santé. These studies were carried out with grants to N.C.C. from the McGill Regenerative Medicine Network, Stem Cell Network (ECR-C4R1-2), The Jesse Davidson Foundation - Defeat Duchenne Canada, and the Canadian Institutes of Health Research (469124).

**Author contributions**
N.C.C. conceived and managed the project. J.A.G., R.R., R.L.F., A.C., S.L. designed and performed experiments, and collected data. J.A.G., R.R., R.L.F., A.C., and N.C.C. analyzed and interpreted the data. M.Y. and J.A.S. contributed bioinformatics analysis. N.C.C. and R.R. wrote the manuscript. All authors carefully reviewed and provided critical insights into the manuscript.

**Competing interests**
The authors declare no competing interests.

**References**


1. Relaix F, Zammit PS. Satellite cells are essential for skeletal muscle regeneration: the cell on the edge returns centre stage. *Development* **139**, 2845-2856 (2012).

2. Mauro A. Satellite cell of skeletal muscle fibers. *The Journal of biophysical and biochemical cytology* **9**, 493 (1961).

3. Le Grand F, Rudnicki MA. Skeletal muscle satellite cells and adult myogenesis. *Current Opinion in Cell Biology* **19**, 628-633 (2007).

4. Sambasivan R*, et al.* Pax7-expressing satellite cells are indispensable for adult skeletal muscle regeneration. *Development* **138**, 3647-3656 (2011).

5. Lepper C, Partridge TA, Fan C-M. An absolute requirement for Pax7-positive satellite cells in acute injury-induced skeletal muscle regeneration. *Development* **138**, 3639-3646 (2011).

6. von Maltzahn J, Jones AE, Parks RJ, Rudnicki MA. Pax7 is critical for the normal function of satellite cells in adult skeletal muscle. *Proceedings of the National Academy of Sciences* **110**, 16474-16479 (2013).

7. Seale P, Sabourin LA, Girgis-Gabardo A, Mansouri A, Gruss P, Rudnicki MA. Pax7 is required for the specification of myogenic satellite cells. *Cell* **102**, 777-786 (2000).

8. García-Prat L*, et al.* FoxO maintains a genuine muscle stem-cell quiescent state until geriatric age. *Nature Cell Biology* **22**, 1307-1318 (2020).

9. Shea KL*, et al.* Sprouty1 regulates reversible quiescence of a self-renewing adult muscle stem cell pool during regeneration. *Cell stem cell* **6**, 117-129 (2010).

10. Fukada S-i*, et al.* Molecular Signature of Quiescent Satellite Cells in Adult Skeletal Muscle. *Stem Cells* **25**, 2448-2459 (2007).

11. Kuang S, Kuroda K, Le Grand F, Rudnicki MA. Asymmetric Self-Renewal and Commitment of Satellite Stem Cells in Muscle. *Cell* **129**, 999-1010 (2007).

12. Zammit PS*, et al.* Pax7 and myogenic progression in skeletal muscle satellite cells. *Journal of Cell Science* **119**, 1824-1832 (2006).

13. Millay DP*, et al.* Myomaker is a membrane activator of myoblast fusion and muscle formation. *Nature* **499**, 301-305 (2013).

14. Bi P*, et al.* Control of muscle formation by the fusogenic micropeptide myomixer. *Science* **356**, 323-327 (2017).

15. Lazure F*, et al.* Myf6/MRF4 is a myogenic niche regulator required for the maintenance of the muscle stem cell pool. *EMBO reports* **21**, e49499 (2020).

16. Zammit PS. Function of the myogenic regulatory factors Myf5, MyoD, Myogenin and MRF4 in skeletal muscle, satellite cells and regenerative myogenesis. In: *Seminars in cell & developmental biology*). Elsevier (2017).

17. Guilhot C, Catenacci M, Lofaro S, Rudnicki MA. The satellite cell in skeletal muscle: A story of heterogeneity. *Current Topics in Developmental Biology* **158**, 15-51 (2024).

18. Tierney MT, Sacco A. Satellite cell heterogeneity in skeletal muscle homeostasis. *Trends in cell biology* **26**, 434-444 (2016).

19. Biressi S, Rando TA. Heterogeneity in the muscle satellite cell population. In: *Seminars in cell & developmental biology*). Elsevier (2010).

20. Rocheteau P, Gayraud-Morel B, Siegl-Cachedenier I, Blasco MA, Tajbakhsh S. A subpopulation of adult skeletal muscle stem cells retains all template DNA strands after cell division. *Cell* **148**, 112-125 (2012).

21. Shinin V, Gayraud-Morel B, Gomès D, Tajbakhsh S. Asymmetric division and cosegregation of template DNA strands in adult muscle satellite cells. *Nature cell biology* **8**, 677-682 (2006).

22. Ono Y, Masuda S, Nam H-s, Benezra R, Miyagoe-Suzuki Y, Takeda Si. Slow-dividing satellite cells retain long-term self-renewal ability in adult muscle. *Journal of Cell Science* **125**, 1309-1317 (2012).

23. Cho DS, Doles JD. Single cell transcriptome analysis of muscle satellite cells reveals widespread transcriptional heterogeneity. *Gene* **636**, 54-63 (2017).

24. Machado L*, et al.* Tissue damage induces a conserved stress response that initiates quiescent muscle stem cell activation. *Cell Stem Cell* **28**, 1125-1135.e1127 (2021).

25. Dell'Orso S*, et al.* Single cell analysis of adult mouse skeletal muscle stem cells in homeostatic and regenerative conditions. *Development* **146**, dev174177 (2019).

26. Oprescu SN, Yue F, Qiu J, Brito LF, Kuang S. Temporal dynamics and heterogeneity of cell populations during skeletal muscle regeneration. *IScience* **23**, (2020).

27. De Micheli AJ*, et al.* Single-cell analysis of the muscle stem cell hierarchy identifies heterotypic communication signals involved in skeletal muscle regeneration. *Cell reports* **30**, 3583-3595. e3585 (2020).

28. Giordani L*, et al.* High-dimensional single-cell cartography reveals novel skeletal muscle-resident cell populations. *Molecular cell* **74**, 609-621. e606 (2019).

29. Walter LD*, et al.* Single-cell transcriptomic analysis of skeletal muscle regeneration across mouse lifespan identifies altered stem cell states associated with senescence. *BioRxiv*, (2023).

30. Conte TC*, et al.* Clearance of defective muscle stem cells by senolytics restores myogenesis in myotonic dystrophy type 1. *Nature Communications* **14**, 4033 (2023).

31. Taglietti V*, et al.* Thyroid-stimulating hormone receptor signaling restores skeletal muscle stem cell regeneration in rats with muscular dystrophy. *Science Translational Medicine* **15**, eadd5275 (2023).

32. Chemello F*, et al.* Degenerative and regenerative pathways underlying Duchenne muscular dystrophy revealed by single-nucleus RNA sequencing. *Proceedings of the National Academy of Sciences* **117**, 29691-29701 (2020).

33. Lazure F*, et al.* Transcriptional reprogramming of skeletal muscle stem cells by the niche environment. *Nature Communications* **14**, 535 (2023).

34. Moiseeva V*, et al.* Senescence atlas reveals an aged-like inflamed niche that blunts muscle regeneration. *Nature* **613**, 169-178 (2023).

35. Emery AE. The muscular dystrophies. *The Lancet* **359**, 687-695 (2002).

36. Mendell JR, Lloyd-Puryear M. Report of MDA muscle disease symposium on newborn screening for Duchenne muscular dystrophy. *Muscle & nerve* **48**, 21-26 (2013).

37. Koenig M, Hoffman E, Bertelson C, Monaco A, Feener C, Kunkel L. Complete cloning of the Duchenne muscular dystrophy (DMD) cDNA and preliminary genomic organization of the DMD gene in normal and affected individuals. *Cell* **50**, 509-517 (1987).

38. Hoffman EP, Brown Jr RH, Kunkel LM. Dystrophin: the protein product of the Duchenne muscular dystrophy locus. *Cell* **51**, 919-928 (1987).

39. Ervasti JM, Campbell KP. Membrane organization of the dystrophin-glycoprotein complex. *Cell* **66**, 1121-1131 (1991).

40. Petrof BJ, Shrager JB, Stedman HH, Kelly AM, Sweeney HL. Dystrophin protects the sarcolemma from stresses developed during muscle contraction. *Proceedings of the National Academy of Sciences* **90**, 3710-3714 (1993).

41. Ervasti JM, Ohlendieck K, Kahl SD, Gaver MG, Campbell KP. Deficiency of a glycoprotein component of the dystrophin complex in dystrophic muscle. *Nature* **345**, 315-319 (1990).

42. Dumont NA*, et al.* Dystrophin expression in muscle stem cells regulates their polarity and asymmetric division. *Nat Med* **21**, 1455-1463 (2015).

43. Chang NC*, et al.* The Dystrophin Glycoprotein Complex Regulates the Epigenetic Activation of Muscle Stem Cell Commitment. *Cell Stem Cell* **22**, 755-768.e756 (2018).

44. Sugihara H*, et al.* Cellular senescence-mediated exacerbation of Duchenne muscular dystrophy. *Scientific Reports* **10**, 16385 (2020).

45. Sacco A*, et al.* Short Telomeres and Stem Cell Exhaustion Model Duchenne Muscular Dystrophy in mdx/mTR Mice. *Cell* **143**, 1059-1071 (2010).

46. Bulfield G, Siller W, Wight P, Moore KJ. X chromosome-linked muscular dystrophy (mdx) in the mouse. *Proceedings of the National Academy of Sciences* **81**, 1189-1192 (1984).

47. Fukada S-i*, et al.* Genetic Background Affects Properties of Satellite Cells and mdx Phenotypes. *The American Journal of Pathology* **176**, 2414-2424 (2010).

48. van Putten M*, et al.* Natural disease history of the D2-mdx mouse model for Duchenne muscular dystrophy. *The FASEB Journal* **33**, 8110-8124 (2019).

49. Saleh KK*, et al.* Single cell sequencing maps skeletal muscle cellular diversity as disease severity increases in dystrophic mouse models. *iScience* **25**, (2022).

50. García-Prat L*, et al.* Autophagy maintains stemness by preventing senescence. *Nature* **529**, 37-42 (2016).

51. Kottlors M, Kirschner J. Elevated satellite cell number in Duchenne muscular dystrophy. *Cell and tissue research* **340**, 541-548 (2010).

52. Bankolé LC, Feasson L, Ponsot E, Kadi F. Fibre type-specific satellite cell content in two models of muscle disease. *Histopathology* **63**, 826-832 (2013).

53. Liu L, Cheung TH, Charville GW, Rando TA. Isolation of skeletal muscle stem cells by fluorescence-activated cell sorting. *Nature protocols* **10**, 1612-1624 (2015).

54. Mourikis P, Sambasivan R, Castel D, Rocheteau P, Bizzarro V, Tajbakhsh S. A Critical Requirement for Notch Signaling in Maintenance of the Quiescent Skeletal Muscle Stem Cell State. *Stem Cells* **30**, 243-252 (2012).

55. Bjornson CRR, Cheung TH, Liu L, Tripathi PV, Steeper KM, Rando TA. Notch Signaling Is Necessary to Maintain Quiescence in Adult Muscle Stem Cells. *Stem Cells* **30**, 232-242 (2012).

56. Engquist EN, Greco A, Joosten LAB, van Engelen BGM, Banerji CRS, Zammit PS. Transcriptomic gene signatures measure satellite cell activity in muscular dystrophies. *iScience* **27**, (2024).

57. Alexander MS*, et al.* CD82 Is a Marker for Prospective Isolation of Human Muscle Satellite Cells and Is Linked to Muscular Dystrophies. *Cell Stem Cell* **19**, 800-807 (2016).

58. Mázala DAG*, et al.* TGF-β–driven muscle degeneration and failed regeneration underlie disease onset in a DMD mouse model. *JCI Insight* **5**, (2020).

59. Cardone N*, et al.* Myopathologic trajectory in Duchenne muscular dystrophy (DMD) reveals lack of regeneration due to senescence in satellite cells. *Acta Neuropathologica Communications* **11**, 167 (2023).

60. Pescatori M*, et al.* Gene expression profiling in the early phases of DMD: a constant molecular signature characterizes DMD muscle from early postnatal life throughout disease progression. *The FASEB Journal* **21**, 1210-1226 (2007).

61. Zhang K, *et al.* Islr regulates canonical Wnt signaling-mediated skeletal muscle regeneration by stabilizing Dishevelled-2 and preventing autophagy. *Nature Communications* **9**, 5129 (2018).

62. Hiramuki Y, Sato T, Furuta Y, Surani MA, Sehara-Fujisawa A. Mest but Not MiR-335 Affects Skeletal Muscle Growth and Regeneration. *PLOS ONE* **10**, e0130436 (2015).

63. Porter JD, *et al.* A chronic inflammatory response dominates the skeletal muscle molecular signature in dystrophin-deficient mdx mice. *Human Molecular Genetics* **11**, 263-272 (2002).

64. Mademtzoglou D, *et al.* Cellular localization of the cell cycle inhibitor Cdkn1c controls growth arrest of adult skeletal muscle stem cells. *eLife* **7**, e33337 (2018).

65. Young LV, *et al.* Muscle injury induces a transient senescence-like state that is required for myofiber growth during muscle regeneration. *The FASEB Journal* **36**, e22587 (2022).

66. Shoji-Kawata S, *et al.* Identification of a candidate therapeutic autophagy-inducing peptide. *Nature* **494**, 201-206 (2013).

67. Wu Y-T, *et al.* Dual Role of 3-Methyladenine in Modulation of Autophagy via Different Temporal Patterns of Inhibition on Class I and III Phosphoinositide 3-Kinase*. *Journal of Biological Chemistry* **285**, 10850-10861 (2010).

68. Taglietti V, *et al.* Duchenne muscular dystrophy trajectory in R-DMDdel52 preclinical rat model identifies COMP as biomarker of fibrosis. *Acta Neuropathologica Communications* **10**, 60 (2022).

69. Yablonka-Reuveni Z, Anderson JE. Satellite cells from dystrophic (Mdx) mice display accelerated differentiation in primary cultures and in isolated myofibers. *Developmental Dynamics* **235**, 203-212 (2006).

70. Boldrin L, Zammit PS, Morgan JE. Satellite cells from dystrophic muscle retain regenerative capacity. *Stem Cell Research* **14**, 20-29 (2015).

71. Blau HM, Webster C, Pavlath GK. Defective myoblasts identified in Duchenne muscular dystrophy. *Proceedings of the National Academy of Sciences* **80**, 4856-4860 (1983).

72. Gosselin MRF, *et al.* Loss of full-length dystrophin expression results in major cell-autonomous abnormalities in proliferating myoblasts. *eLife* **11**, e75521 (2022).

73. Fiacco E, *et al.* Autophagy regulates satellite cell ability to regenerate normal and dystrophic muscles. *Cell Death & Differentiation* **23**, 1839-1849 (2016).

74. Spitali P, Grumati P, Hiller M, Chrisam M, Aartsma-Rus A, Bonaldo P. Autophagy is Impaired in the Tibialis Anterior of Dystrophin Null Mice. *PLoS Curr* **5**, (2013).

75. De Palma C, *et al.* Autophagy as a new therapeutic target in Duchenne muscular dystrophy. *Cell Death & Disease* **3**, e418-e418 (2012).

76. Pauly M, *et al.* AMPK Activation Stimulates Autophagy and Ameliorates Muscular Dystrophy in the mdx Mouse Diaphragm. *The American Journal of Pathology* **181**, 583-592 (2012).

77. Bibee KP, *et al.* Rapamycin nanoparticles target defective autophagy in muscular dystrophy to enhance both strength and cardiac function. *The FASEB Journal* **28**, 2047-2061 (2014).

78. Schindelin J, *et al.* Fiji: an open-source platform for biological-image analysis. *Nature Methods* **9**, 676-682 (2012).

79. Encarnacion-Rivera L, Foltz S, Hartzell HC, Choo H. Myosoft: An automated muscle histology analysis tool using machine learning algorithm utilizing FIJI/ImageJ software. *PLOS ONE* **15**, e0229041 (2020).

80. Pasut A, Oleynik P, Rudnicki MA. Isolation of Muscle Stem Cells by Fluorescence Activated Cell Sorting Cytometry. In: *Myogenesis: Methods and Protocols* (ed DiMario JX). Humana Press (2012).

81. Hao Y, *et al.* Dictionary learning for integrative, multimodal and scalable single-cell analysis. *Nature Biotechnology* **42**, 293-304 (2024).

82. McGinnis CS, Murrow LM, Gartner ZJ. DoubletFinder: Doublet Detection in Single-Cell RNA Sequencing Data Using Artificial Nearest Neighbors. *Cell Systems* **8**, 329-337.e324 (2019).

83. Zappia L, Oshlack A. Clustering trees: a visualization for evaluating clusterings at multiple resolutions. *Gigascience* **7**, (2018).

84. Lin I-H. StackedVlnPlot, https://github.com/ycl6/StackedVlnPlot?tab=readme-ov-file#stackedvlnplot (2020).

85. Marsh S. scCustomize: Custom Visualizations & Functions for Streamlined Analyses of Single Cell Sequencing, 2.1.2, https://samuel-marsh.github.io/scCustomize/ (2024).

86. Ratcliff J, Thurman A. aggregateBioVar: Differential Gene Expression Analysis for Multi-subject scRNA-seq, 1.14.0, https://github.com/jasonratcliff/aggregateBioVar (2024).

87. Love MI, Huber W, Anders S. Moderated estimation of fold change and dispersion for RNA-seq data with DESeq2. *Genome Biology* **15**, 550 (2014).

88. Zhou Y, *et al.* Metascape provides a biologist-oriented resource for the analysis of systems-level datasets. *Nature Communications* **10**, 1523 (2019).

89. Wu T, *et al.* clusterProfiler 4.0: A universal enrichment tool for interpreting omics data. *The Innovation* **2**, (2021).

90. Blighe K, Rana S, Lewis M. EnhancedVolcano, 1.22.0, (2024).

91. Chen H. VennDiagram package, 1.7.3, https://rdrr.io/cran/VennDiagram/ (2022).

92. Cao J*, et al.* The single-cell transcriptional landscape of mammalian organogenesis. *Nature* **566**, 496-502 (2019).

93. Filippelli RL, Omer A, Li S, van Oostende-Triplet C, Gallouzi IE, Chang NC. Automated Quantification of Subcellular Particles in Myogenic Progenitors. *Current Protocols* **1**, e325 (2021).

94. VanGenderen CA, Granet JA, Filippelli RL, Liu Y, Chang NC. Modulating Myogenesis: An Optimized In Vitro Assay to Pharmacologically Influence Primary Myoblast Differentiation. *Current Protocols* **2**, e565 (2022).

Figure 1

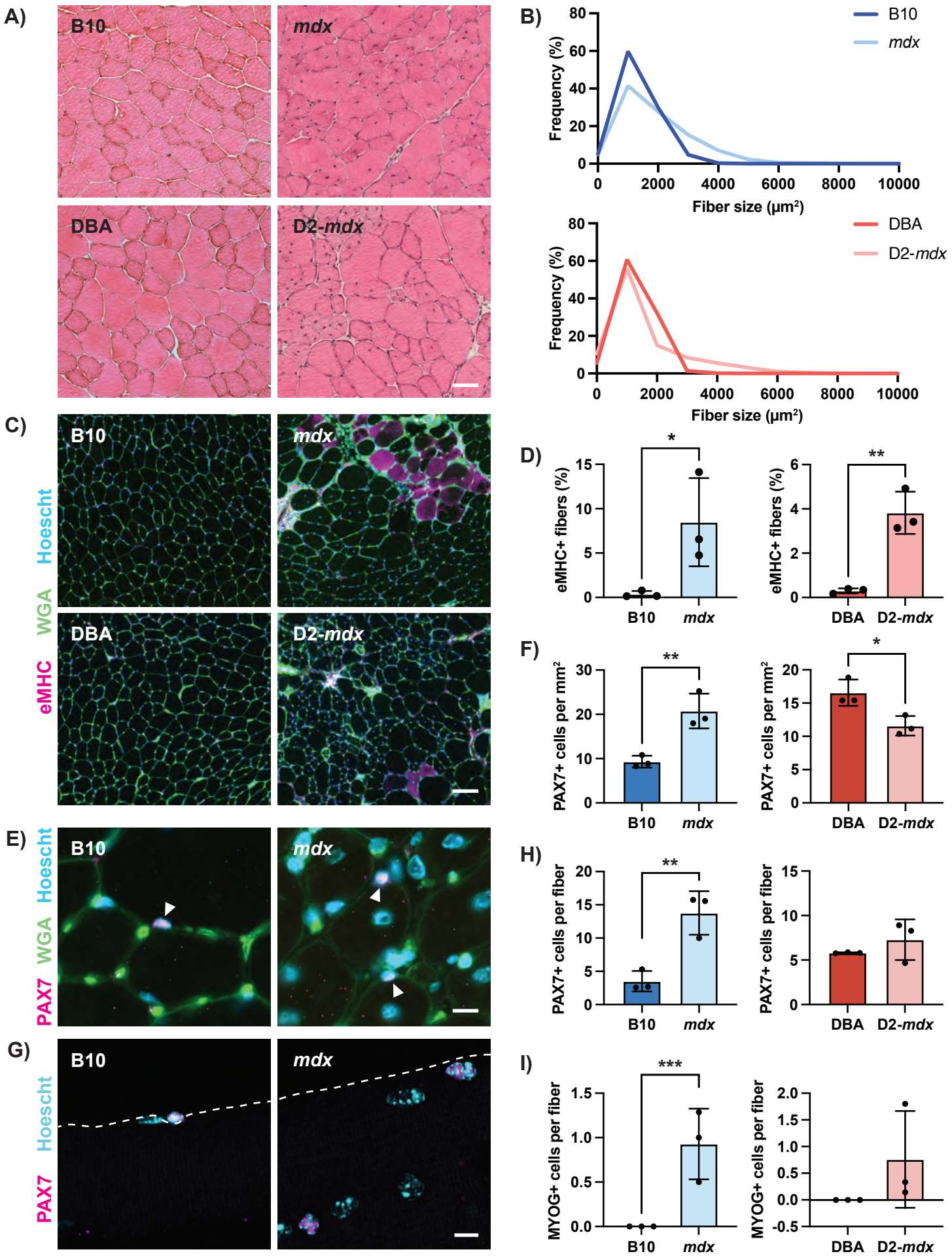
A)
B10
mdx
DBA
D2-mdx
B)
B10
mdx
Frequency (%)
Fiber size (µm²)
DBA
D2-mdx
C)
Hoescht
WGA
eMHC
D)
eMHC+ fibers (%)
E)
PAX7
F)
PAX7+ cells per mm²
H)
PAX7+ cells per fiber
G)
I)
MYOG+ cells per fiber

## Figure 2

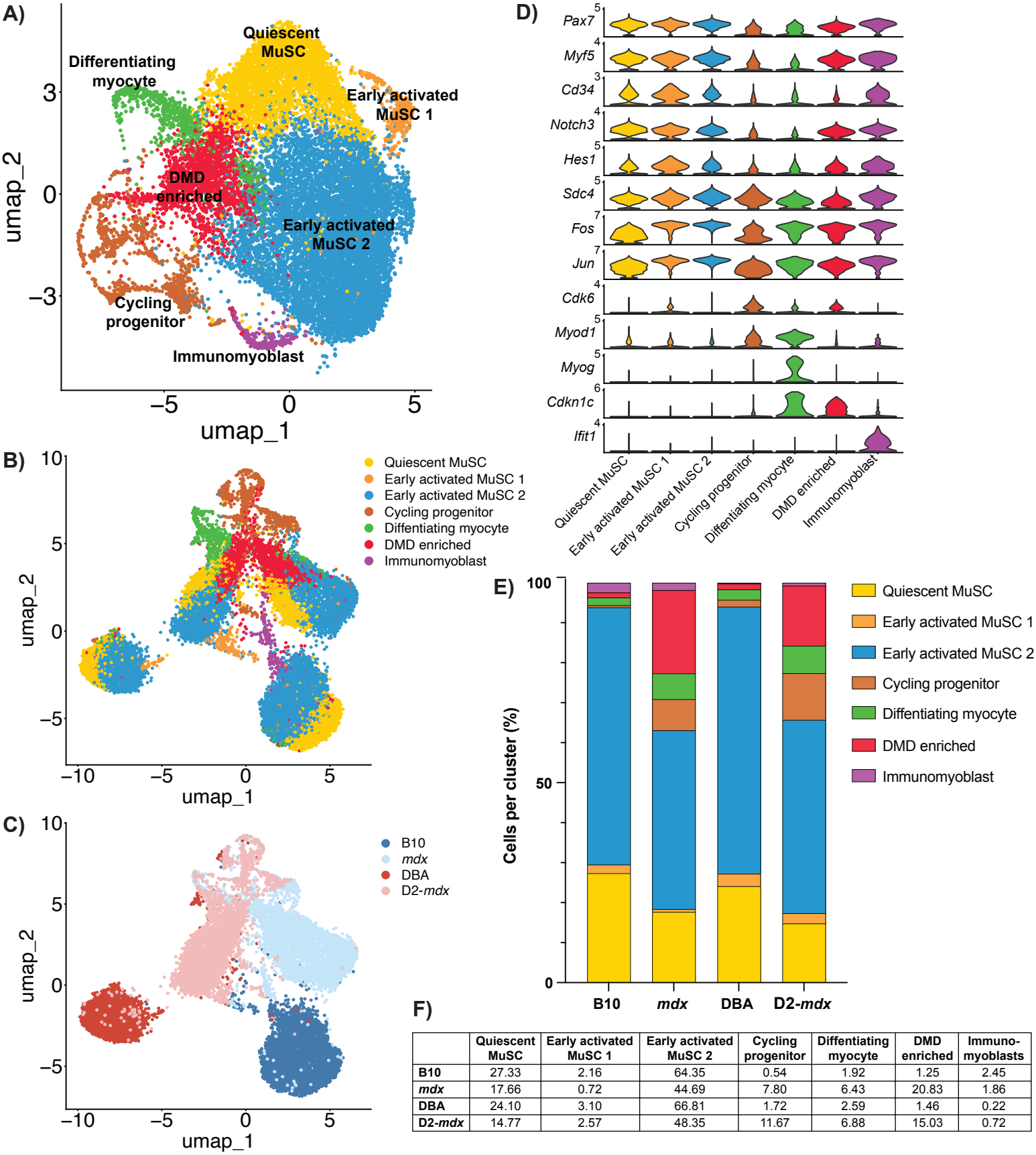


F)

| | Quiescent MuSC | Early activated MuSC 1 | Early activated MuSC 2 | Cycling progenitor | Diffentiating myocyte | DMD enriched | Immuno-myoblasts |
|---|---|---|---|---|---|---|---|
| **B10** | 27.33 | 2.16 | 64.35 | 0.54 | 1.92 | 1.25 | 2.45 |
| ***mdx*** | 17.66 | 0.72 | 44.69 | 7.80 | 6.43 | 20.83 | 1.86 |
| **DBA** | 24.10 | 3.10 | 66.81 | 1.72 | 2.59 | 1.46 | 0.22 |
| **D2-*mdx*** | 14.77 | 2.57 | 48.35 | 11.67 | 6.88 | 15.03 | 0.72 |

## Figure 3

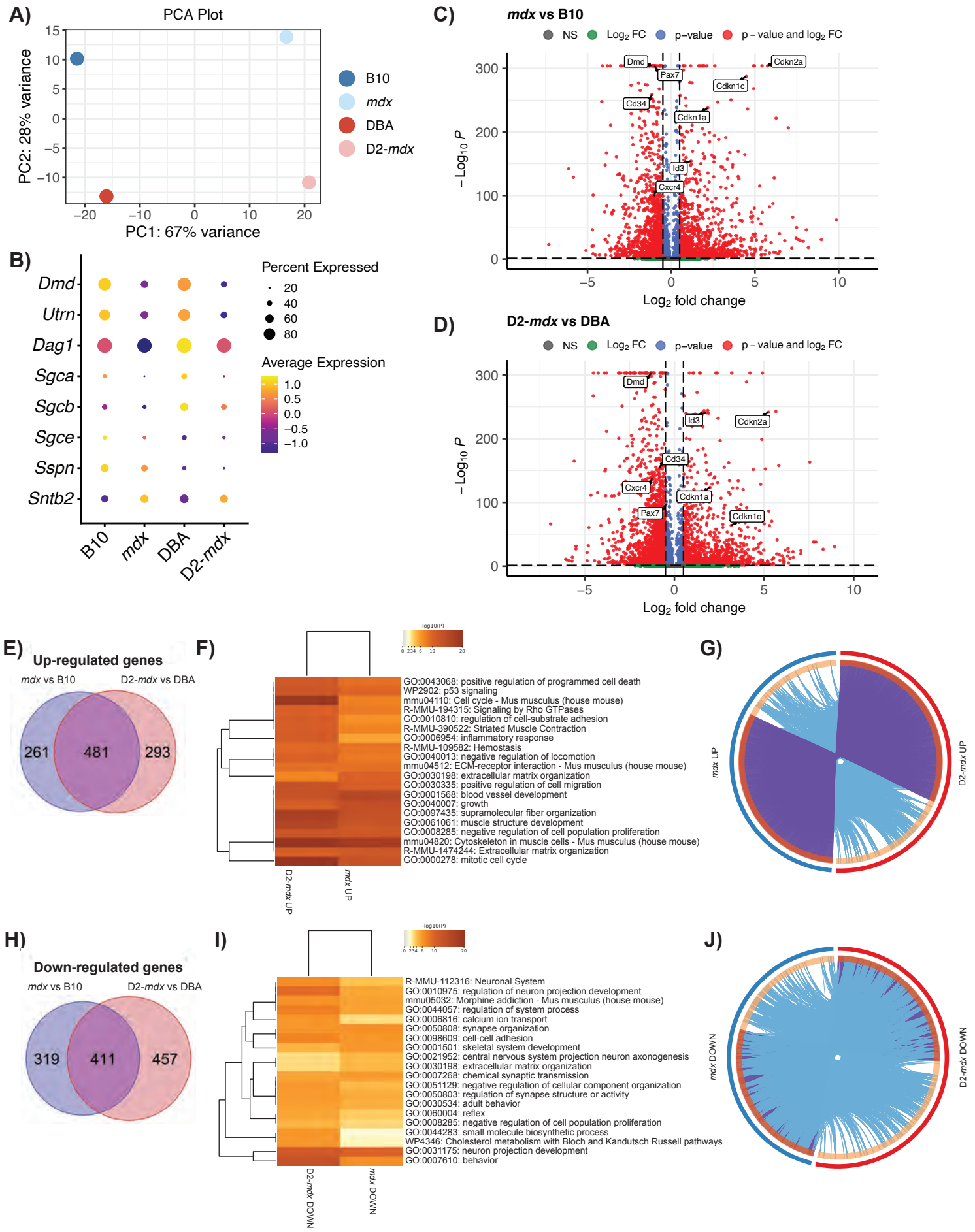
A)
PCA Plot
PC2: 28% variance
PC1: 67% variance
B10
mdx
DBA
D2-mdx
B)
Dmd
Utrn
Dag1
Sgca
Sgcb
Sgce
Sspn
Sntb2
B10
mdx
DBA
D2-mdx
Percent Expressed
20
40
60
80
Average Expression
1.0
0.5
0.0
−0.5
−1.0
C)
mdx vs B10
NS
Log2 FC
p−value
p − value and log2 FC
−Log10 P
Log2 fold change
Dmd
Pax7
Cdkn2a
Cdkn1c
Cd34
Cdkn1a
Id3
Cxcr4
D)
D2-mdx vs DBA
NS
Log2 FC
p−value
p − value and log2 FC
−Log10 P
Log2 fold change
Dmd
Id3
Cdkn2a
Cd34
Cxcr4
Cdkn1a
Pax7
Cdkn1c
E)
Up-regulated genes
mdx vs B10
D2-mdx vs DBA
261
481
293
F)
-log10(P)
GO:0043068: positive regulation of programmed cell death
WP2902: p53 signaling
mmu04110: Cell cycle - Mus musculus (house mouse)
R-MMU-194315: Signaling by Rho GTPases
GO:0010810: regulation of cell-substrate adhesion
R-MMU-390522: Striated Muscle Contraction
GO:0006954: inflammatory response
R-MMU-109582: Hemostasis
GO:0040013: negative regulation of locomotion
mmu04512: ECM-receptor interaction - Mus musculus (house mouse)
GO:0030198: extracellular matrix organization
GO:0030335: positive regulation of cell migration
GO:0001568: blood vessel development
GO:0040007: growth
GO:0097435: supramolecular fiber organization
GO:0061061: muscle structure development
GO:0008285: negative regulation of cell population proliferation
mmu04820: Cytoskeleton in muscle cells - Mus musculus (house mouse)
R-MMU-1474244: Extracellular matrix organization
GO:0000278: mitotic cell cycle
D2-mdx UP
mdx UP
G)
mdx UP
D2-mdx UP
H)
Down-regulated genes
mdx vs B10
D2-mdx vs DBA
319
411
457
I)
-log10(P)
R-MMU-112316: Neuronal System
GO:0010975: regulation of neuron projection development
mmu05032: Morphine addiction - Mus musculus (house mouse)
GO:0044057: regulation of system process
GO:0006816: calcium ion transport
GO:0050808: synapse organization
GO:0098609: cell-cell adhesion
GO:0001501: skeletal system development
GO:0021952: central nervous system projection neuron axonogenesis
GO:0030198: extracellular matrix organization
GO:0007268: chemical synaptic transmission
GO:0051129: negative regulation of cellular component organization
GO:0050803: regulation of synapse structure or activity
GO:0030534: adult behavior
GO:0060004: reflex
GO:0008285: negative regulation of cell population proliferation
GO:0044283: small molecule biosynthetic process
WP4346: Cholesterol metabolism with Bloch and Kandutsch Russell pathways
GO:0031175: neuron projection development
GO:0007610: behavior
D2-mdx DOWN
mdx DOWN
J)
mdx DOWN
D2-mdx DOWN

## Figure 4

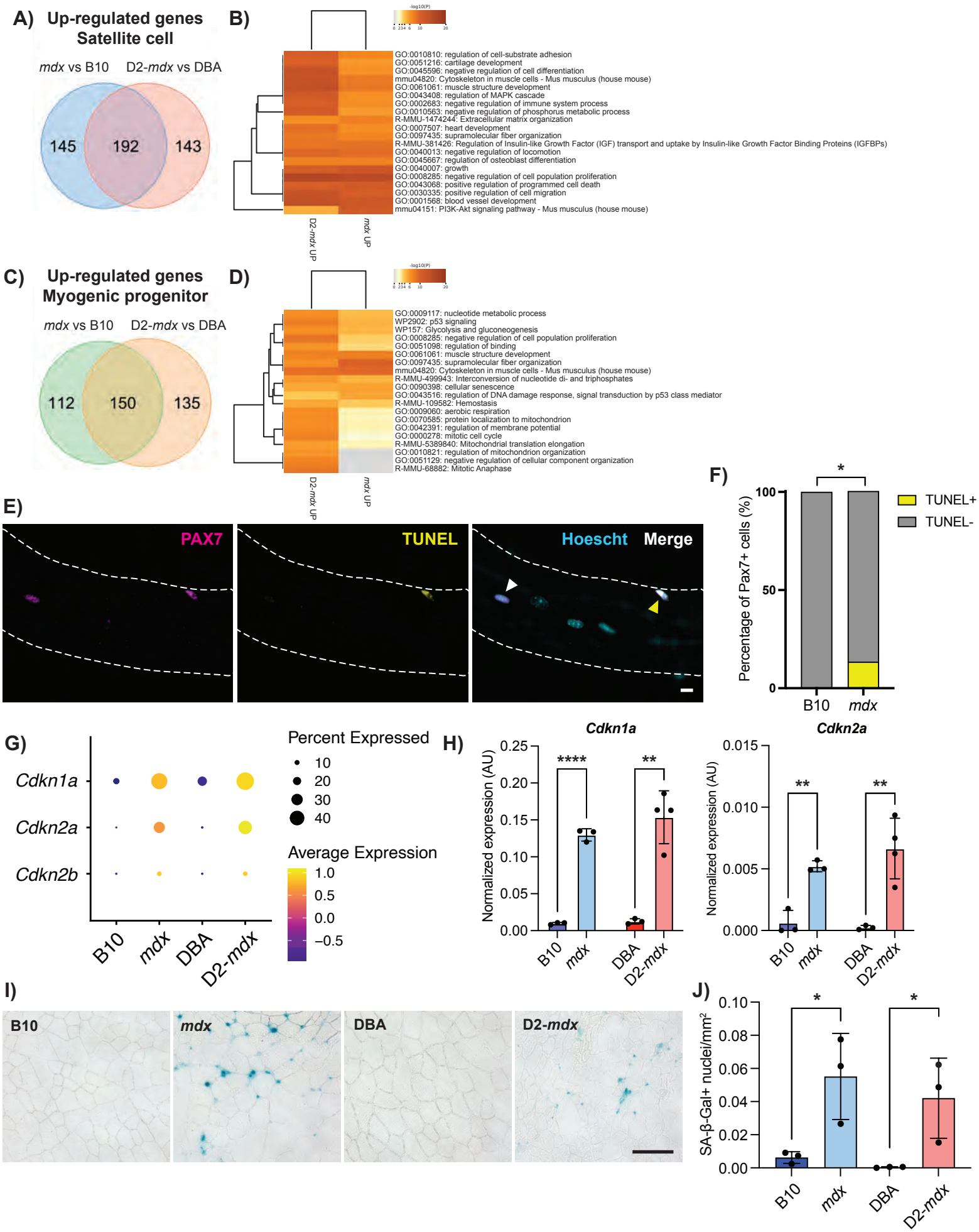
A) Up-regulated genes Satellite cell
mdx vs B10
D2-mdx vs DBA
145
192
143
B)
-log10(P)
GO:0010810: regulation of cell-substrate adhesion
GO:0051216: cartilage development
GO:0045596: negative regulation of cell differentiation
mmu04820: Cytoskeleton in muscle cells - Mus musculus (house mouse)
GO:0061061: muscle structure development
GO:0043408: regulation of MAPK cascade
GO:0002683: negative regulation of immune system process
GO:0010563: negative regulation of phosphorus metabolic process
R-MMU-1474244: Extracellular matrix organization
GO:0007507: heart development
GO:0097435: supramolecular fiber organization
R-MMU-381426: Regulation of Insulin-like Growth Factor (IGF) transport and uptake by Insulin-like Growth Factor Binding Proteins (IGFBPs)
GO:0040013: negative regulation of locomotion
GO:0045667: regulation of osteoblast differentiation
GO:0040007: growth
GO:0008285: negative regulation of cell population proliferation
GO:0043068: positive regulation of programmed cell death
GO:0030335: positive regulation of cell migration
GO:0001568: blood vessel development
mmu04151: PI3K-Akt signaling pathway - Mus musculus (house mouse)
D2-mdx UP
mdx UP
C) Up-regulated genes Myogenic progenitor
mdx vs B10
D2-mdx vs DBA
112
150
135
D)
-log10(P)
GO:0009117: nucleotide metabolic process
WP2902: p53 signaling
WP157: Glycolysis and gluconeogenesis
GO:0008285: negative regulation of cell population proliferation
GO:0051098: regulation of binding
GO:0061061: muscle structure development
GO:0097435: supramolecular fiber organization
mmu04820: Cytoskeleton in muscle cells - Mus musculus (house mouse)
R-MMU-499943: Interconversion of nucleotide di- and triphosphates
GO:0090398: cellular senescence
GO:0043516: regulation of DNA damage response, signal transduction by p53 class mediator
R-MMU-109582: Hemostasis
GO:0009060: aerobic respiration
GO:0070585: protein localization to mitochondrion
GO:0042391: regulation of membrane potential
GO:0000278: mitotic cell cycle
R-MMU-5389840: Mitochondrial translation elongation
GO:0010821: regulation of mitochondrion organization
GO:0051129: negative regulation of cellular component organization
R-MMU-68882: Mitotic Anaphase
D2-mdx UP
mdx UP
E)
PAX7
TUNEL
Hoescht
Merge
F)
Percentage of Pax7+ cells (%)
100
50
0
*
TUNEL+
TUNEL-
B10
mdx
G)
Cdkn1a
Cdkn2a
Cdkn2b
B10
mdx
DBA
D2-mdx
Percent Expressed
10
20
30
40
Average Expression
1.0
0.5
0.0
−0.5
H)
Cdkn1a
Normalized expression (AU)
0.25
0.20
0.15
0.10
0.05
0.00
****
**
B10
mdx
DBA
D2-mdx
Cdkn2a
Normalized expression (AU)
0.015
0.010
0.005
0.000
**
**
B10
mdx
DBA
D2-mdx
I)
B10
mdx
DBA
D2-mdx
J)
SA-β-Gal+ nuclei/mm²
0.10
0.08
0.06
0.04
0.02
0.00
*
*
B10
mdx
DBA
D2-mdx

# Figure 5

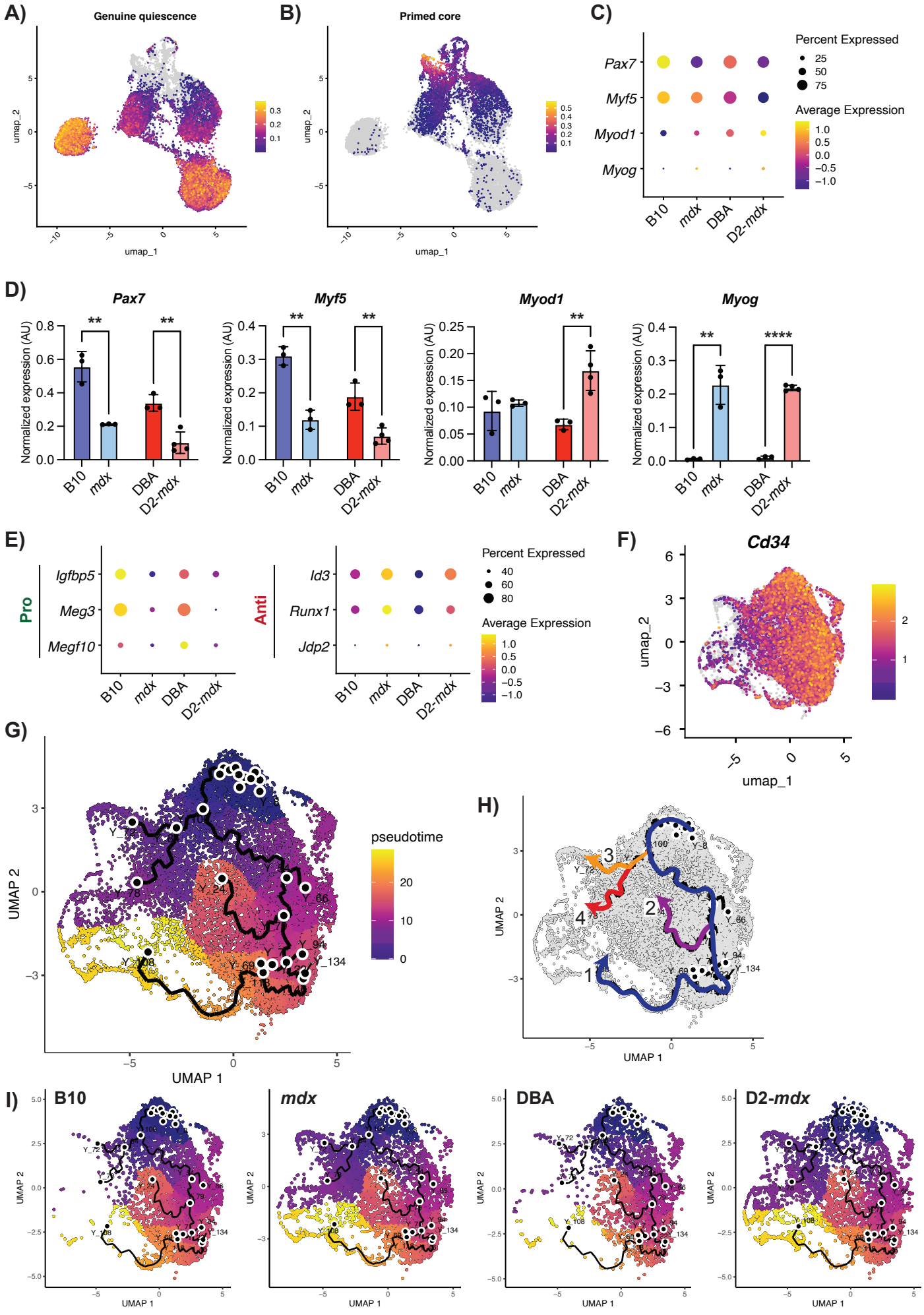
A)
Genuine quiescence
umap_1
umap_2
B)
Primed core
C)
Pax7
Myf5
Myod1
Myog
B10
mdx
DBA
D2-mdx
Percent Expressed
25
50
75
Average Expression
1.0
0.5
0.0
−0.5
−1.0
D)
Pax7
Myf5
Myod1
Myog
Normalized expression (AU)
**
****
E)
Pro
Igfbp5
Meg3
Megf10
Anti
Id3
Runx1
Jdp2
F)
Cd34
G)
pseudotime
UMAP 1
UMAP 2
H)
1
2
3
4
I)
B10
mdx
DBA
D2-mdx

**Figure 6**

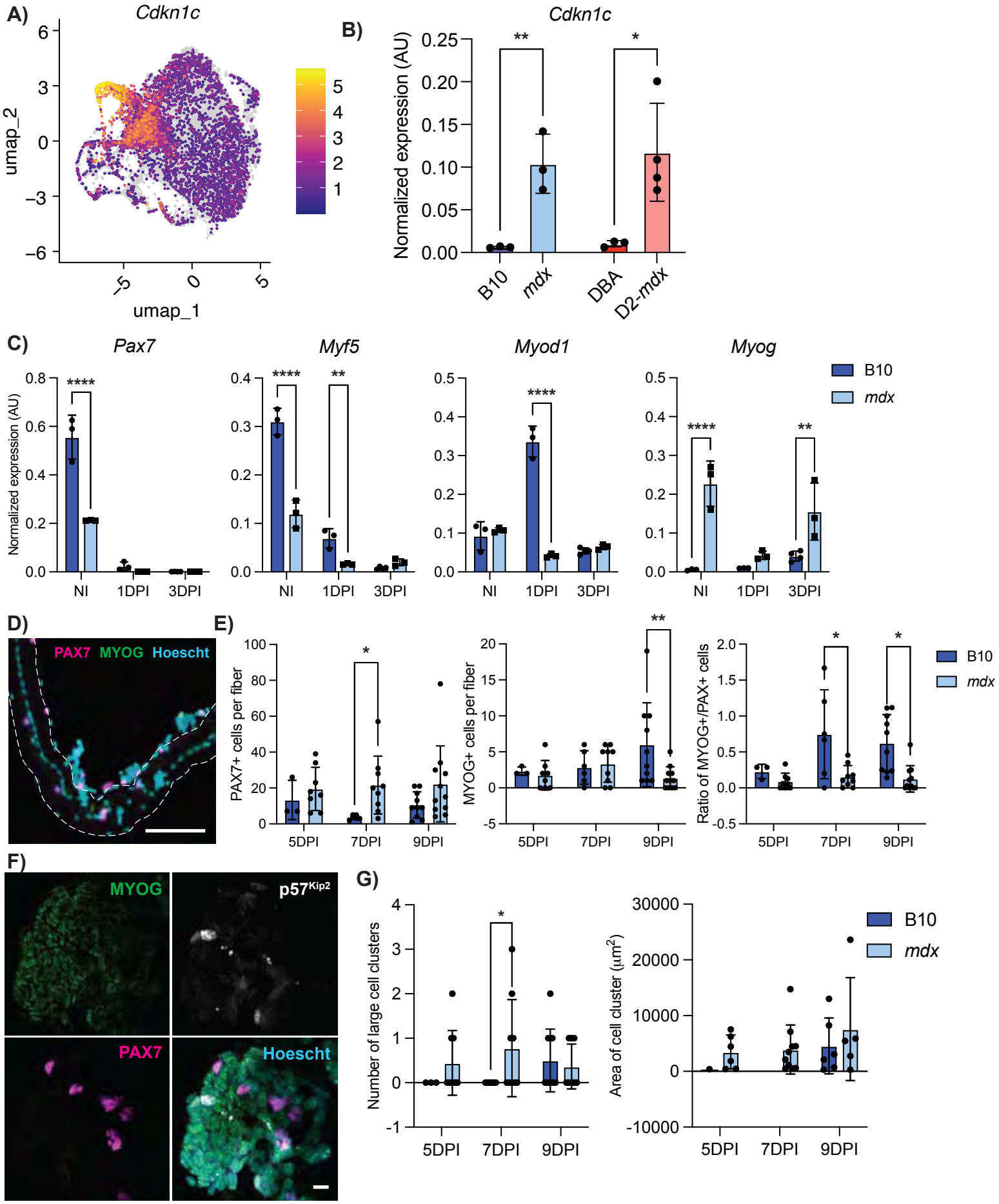
A)
Cdkn1c
umap_2
umap_1
B)
Cdkn1c
Normalized expression (AU)
B10
mdx
DBA
D2-mdx
C)
Pax7
Myf5
Myod1
Myog
Normalized expression (AU)
NI
1DPI
3DPI
B10
mdx
D)
PAX7 MYOG Hoescht
E)
PAX7+ cells per fiber
MYOG+ cells per fiber
Ratio of MYOG+/PAX+ cells
5DPI
7DPI
9DPI
B10
mdx
F)
MYOG
p57Kip2
PAX7
Hoescht
G)
Number of large cell clusters
Area of cell cluster (μm2)
5DPI
7DPI
9DPI
B10
mdx

**Figure 7**

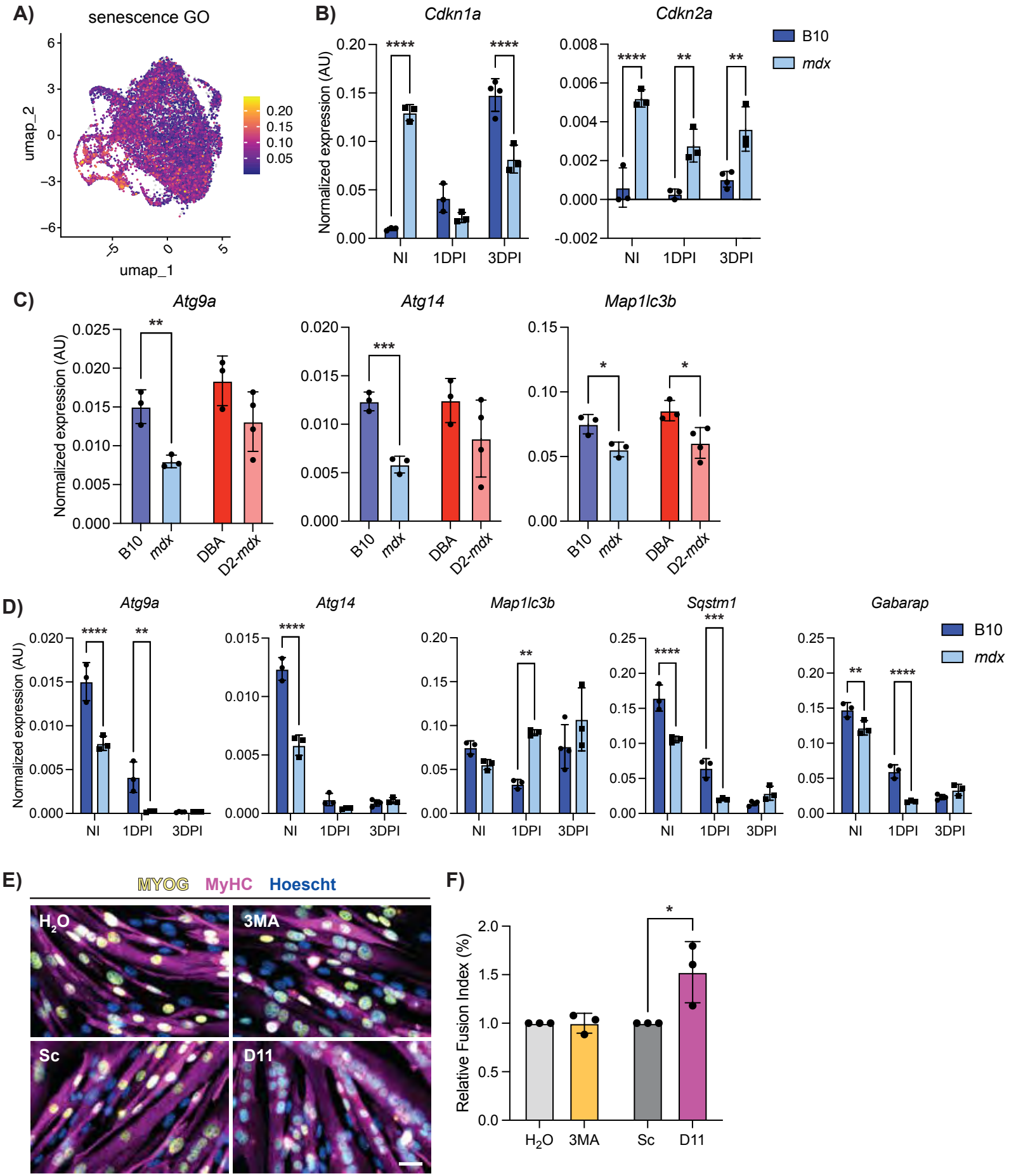
A)
senescence GO
umap_2
umap_1
0.20
0.15
0.10
0.05
B)
Cdkn1a
Cdkn2a
Normalized expression (AU)
B10
mdx
NI
1DPI
3DPI
C)
Atg9a
Atg14
Map1lc3b
B10
mdx
DBA
D2-mdx
D)
Atg9a
Atg14
Map1lc3b
Sqstm1
Gabarap
E)
MYOG
MyHC
Hoescht
H2O
3MA
Sc
D11
F)
Relative Fusion Index (%)
H2O
3MA
Sc
D11

**Figure Legends**

**Figure 1.** Altered regenerative and satellite cell profiles in *mdx* and D2-*mdx* mice. **A)** H&E images from TA cross-sections of three-month old male DMD models (*mdx* and D2-*mdx)* and their respective controls (B10 and DBA), showing morphological changes in the DMD models such as centralized nuclei and changes in fiber cross sectional area. **B)** Quantification of fiber cross sectional area, demonstrating changes in DMD models compared to controls. **C)** Representative WGA (green) and eMHC (magenta) IF labelling of TA cross-sections which, as quantified in **D)** shows a significant increase in eMHC+ fibers in DMD models compared to controls (t = 2.817, 6.337, respectively). **E)** Representative IF labelling of TA cross-sections for WGA (green) and PAX7 (magenta), showing PAX7+ satellite cells (arrows). **F)** Quantification of number of PAX7+ cells per $mm^2$ of TA, showing a significant increase in *mdx* and a decrease D2-*mdx* compared to their respective controls. (t = 3.516, 4.780) **G)** Single EDL myofibers labelled for PAX7 (magenta). **H, I)** Quantification of PAX7+ (**H**) and MYOG+ (**I**) cells per myofiber showing a significant increase of both in *mdx* (t = 4.851 (**H**), 4.145 (**I**)) but no significant change in D2-*mdx* (t = 1.425 (**H**), 1.489 (**I**)) as compared to respective controls. Scalebars = 50 µm, *P < 0.05, **P < 0.01, ***P < 0.001 (two-tailed unpaired t-test, n = 3 biological replicates per strain, df = 4). Data are expressed as frequency distribution (**B**) or mean ± SD (**D, F, H, I**)

**Figure 2.** Single cell RNA-seq analysis of DMD satellite cells. **A)** UMAP representation after clustering of myogenic cells using the "FindNeighbours" algorithm showing the mapping of cells into seven distinct clusters and **B)** UMAP representation using the same resolution without the "FindNeighbours" algorithm, labelled by cell type and **C)** labelled by strain. **D)** Violin plot of highly expressed markers used to define the identity of each myogenic cluster. **E)** Percentage of cells belonging to each cluster by strain, summarized in **F)**, showing a decrease in quiescent and early activated muscle stem cells (MuSC) and increase in cycling, differentiating and "DMD enriched" clusters in the DMD models *mdx* and D2-*mdx* compared to their respective controls.

**Figure 3.** Differential gene expression in DMD satellite cells. **A)** PCA plot showing separation of DMD models versus healthy controls across PC1 and mouse genetic background on PC2. **B)** Dot plot of the expression of genes which comprise the dystrophin-glycoprotein complex, showing decreased expression of all components except *Sntb2* in DMD models vs respective controls. **C, D)** Volcano plots of differentially expressed genes in *mdx* versus B10 (**C**) and D2-*mdx* versus DBA (**D**). **E, H)** Venn diagram of up-regulated (**E**) and down-regulated (**H**) genes from *mdx* versus B10 (blue) and D2-*mdx* versus DBA (pink) and their overlap and **F, I)** heatmaps of top 20 enriched GO terms, coloured by p-value, related to these gene lists. **G, J)** Circos plots representing overlap between up-regulated (**G**) and down-regulated (**J**) gene lists. Outer circle represents the gene list for *mdx* (blue) and D2-*mdx* (red). Inner circle represents gene lists, where hits are arranged along the arc. Genes that hit multiple lists are colored in dark orange, and genes unique to a list are shown in light orange. Purple curves link identical genes between gene lists. Blue curves link genes that belong to the same enriched ontology term.

**Figure 4.** Apoptosis in DMD satellite cells and senescence in DMD myogenic progenitors. **A-D)** Comparison of most up-regulated genes (**A, C**) and heatmaps of top 20 enriched GO terms related to these genes (**B, D**) from *mdx* versus B10 and D2-*mdx* versus DBA within both satellite cells (**A-B**) and myogenic progenitors (**C-D**). **E)** Representative IF labelling of an uninjured *mdx* EDL myofiber for PAX7 (magenta) and TUNEL (yellow) showing a nucleus for PAX7 only (white arrow) and a nucleus double positive for both PAX7 and TUNEL (yellow arrow). **F)** Quantification of number of total PAX7+ nuclei (n = 25 B10, n = 82 *mdx*) that are positive for TUNEL, visualized as a percentage, showing their presence in *mdx* only. **G)** Dot plot of scRNA-seq data showing an increase in

senescence-associated genes *Cdkn1a*, *Cdkn2a* and *Cdkn2b* in DMD models as compared to controls and **H)** verification of this increase in *Cdkn1a* (t = 24.53, 6.621) and *Cdkn2a* (t =7 .208, 4.40) with ddPCR. **I)** SA-β-Gal staining of TA cross-sections showing senescence in DMD models and **J)** quantification of SA-β-Gal+ nuclei showing significant increase in DMD muscle as compared to controls (t = 3.230, 2.986). Scalebars = 10 µm (**E**), 100 µm (**I**). *P < 0.05, **P < 0.01, ****P < 0.0001 (two-tailed unpaired t-test (**H, J**), one-sided Fisher's exact test (**F**)). Data are expressed as mean ± SD (**H, J**) unless otherwise noted.

**Figure 5.** DMD MuSCs exhibit impaired myogenic differentiation. Feature plot of **A)** genuine quiescence signature, with more expression in areas representing healthy control animals and **B)** primed core signature with more expression in areas representing DMD models. **C)** Dot plot of scRNA-seq data and **D)** ddPCR validation showing changes in expression of myogenic factors in DMD models, showing lowered expression of early satellite cell factors like *Pax7* and increased expression of late differentiation factors such as *Myog.* (in order, t = 6.560, 5.287; 8.321, 4.833; 0.6940, 4.494; 6.575, 40.05; **P < 0.01, ****P < 0.0001 (two-tailed unpaired t-test)). Data are expressed as mean ± SD. **E)** Dot plot of scRNA-seq data for regulators of differentiation showing a decrease in pro-differentiation and an increase in anti-differentiation genes in DMD models compared to controls. **F)** Feature plot of *Cd34* showing higher expression in areas which are more quiescent and early-activated. **G)** Pseudotime analysis of satellite cells showing cell fate trajectory with **H)** four distinct cell fates, and **I)** visualization by strain showing a preference for the "DMD enriched cluster" fate (4) in DMD compared to control satellite cells.

**Figure 6.** DMD satellite cells exhibit impaired *in vivo* regenerative myogenesis. **A)** Feature plot of *Cdkn1c* showing increased expression in areas representing DMD-enriched and differentiating myocyte clusters. **B)** ddPCR validation of *Cdkn1c* expression showing significant increase in DMD models compared to their respective controls (F = 18.09, P = 0.0002). **C)** Expression of myogenic factors in satellite cells from non-injured (NI), one-day post-injury (1DPI) and three-day post-injury (3DPI) showing dysregulation in *mdx* mice during myogenesis. ([F,P] = [43.45, <0.0001], [54.08, <0.0001], [99.87, <0.0001], [9.542, 0.0028]) **D)** Representative IF labelling of an *mdx* EDL myofiber isolated 7-days post-injury for PAX7 (magenta) and MYOG (green), showing myogenic clusters along the fiber. **E)** Quantification of PAX7+ and MYOG+ nuclei at 5, 7 and 9 DPI showing more PAX7+ and less MYOG+ nuclei in *mdx*. (Strain x DPI interaction: F = 0.4930, P = 0.6144; strain factor: F = 6.839, P = 0.0124 (PAX7) and F = 4.006, P = 0.038 (MYOG)) **F)** A large myogenic cluster labelled for MYOG, $p57^{Kip2}$ and PAX7 and **G)** quantification of the number of large clusters (> 1000 $\mu m^2$) and the area of these clusters (F = 2.196, P = 0.1323; F = 0.4316, P = 0.6523). Scalebars = 100 µm (**D**), 10 µm (**F**). *P < 0.05, **P < 0.01, ****P < 0.0001 (two-tailed unpaired t-test (**B, E, G**) or mixed-effects analysis (**C**)). Data are expressed as mean ± SD.

**Figure 7**. DMD satellite cells have impaired autophagy and senescence. **A)** Feature plot showing cells positive for the senescence GO term, showing higher amounts in the regions where cycling progenitors and DMD enriched cells cluster. **B-D)** ddPCR quantification of gene expression in satellite cells in **B)** senescence-associated genes *Cdkn1a* and *Cdkn2a* from non-injured (NI), one day post injury (1DPI) and three days post injury (3DPI) B10 and *mdx* mice showing dysregulation in *mdx*. (F = 101.1, P < 0.0001; F = 89.58, P < 0.0001) **C)** Strain-comparison of the expression of autophagy-associated genes showing reduced expression of autophagy genes in both DMD models compared to healthy controls (t = 5.260, 1.917; 8.707, 1.513; 3.603, 3.130) and **D)** changes in autophagy-associated genes in NI, 1DPI and 3DPI B10 and *mdx* satellite cells demonstrating impaired autophagy dynamics in *mdx* cells during regeneration ([F,P] = [15.51, 0.0004], [62.45, 0.0001], [6.518, 0.0109], [24.28, <0.0001], [20.22,

0.0001]. **E)** Representative images of IF staining against PAX7, MYOG and MyHC from *mdx* primary myoblasts treated with an autophagy inhibitor (3-MA, 5 mM and $H_2O$ control) or autophagy inducer (Tat-D11, 10 μM and Scramble control) for two hours prior to differentiation for two days. **F)** Fusion index of each condition was determined and shows increased differentiation after Tat-D11 treatment (t = 0.001 (3MA), 2.894 (Tat-D11)). Scalebars = 25 μM, *P < 0.05, **P < 0.01, ***P < 0.001, ****P < 0.0001 (two-tailed unpaired t-test (**C, F**) and two-way analysis of variance (**B, D**)). Data are expressed as mean ± SD.